UNIVERSITY OF HELSINKI REPORT SERIES IN PHYSICS

HU-P-D223

# STRUCTURAL STUDIES FROM NANOSCALE TO MACROSCALE WITH X-RAY MICROTOMOGRAPHY AND MICROBEAM SCATTERING

**Jussi-Petteri Suuronen**

Division of Materials Physics
Department of Physics
Faculty of Science
University of Helsinki
Helsinki, Finland

*ACADEMIC DISSERTATION*

*To be presented, with the permission of the Faculty of Science of the University of Helsinki, for public examination in Theatre 5 of the main building of the University of Helsinki, Fabianinkatu 33, on 13th of December 2014 at 10 o'clock AM.*

Helsinki 2014

**Supervisor**

Prof. Ritva Serimaa
Department of Physics
University of Helsinki
Helsinki, Finland

**Pre-examiners**

Prof. Markku Kataja
Department of Physics
University of Jyväskylä
Jyväskylä, Finland

Dr. Anders Kaestner
Laboratory for Neutron Scattering and Imaging
Paul Scherrer Institute
Villigen, Switzerland

**Opponent**

Prof. Jean-Yves Buffière
Laboratoire MATEIS
Institut National des Sciences Appliquées
Lyon, France

**Custos**

Prof. Keijo Hämäläinen
Department of Physics
University of Helsinki
Helsinki, Finland

Report Series in Physics HU-P-D223
ISSN 0356-0961
ISBN 978-952-10-8973-2 (printed version)
ISBN 978-952-10-8974-9 (pdf version)
http://ethesis.helsinki.fi/
Picaset Oy
Helsingin Yliopiston verkkojulkaisut
Helsinki 2014

# Preface

Like science in general, this thesis could not have been accomplished by only one person, but is the cumulative sum of my own input and the innumerable discussions, ideas, data, snippets of code, and coffee-fueled late night writing sessions contributed by others. I owe my deepest gratitude to great many people for their help, encouragement and support.

The work presented in this thesis was carried out at the Department of Physics, University of Helsinki. I thank the current and previous Department heads, Prof. Juhani Keinonen and Prof. Hannu Koskinen for the opportunity to work at Division of Materials Physics. All of my co-authors deserve recognition for their part in the included papers: I will mention especially M.Sc. Michal Matusewicz from VTT for his assistance in the field of bentonite, Dr. Heiko Herrmann from the Tallinn University of Technology and Dr. Marika Eik from Aalto University for the concrete collaboration, Dr. Henrik Mauroy from IFE for the work on polymer-clay nanocomposites and Dr. Tomas Kohout, whom the Department's organizational upheavals eventually landed in our Division, for his expertise in the micrometeorite business.

My supervisor, Prof. Ritva Serimaa is the person who recruited me in the first place, and gently steered this thesis project in the right direction. I thank her for her patience and advice, and for the freedom to pursue my own interests and find my own way while putting the thesis together. Valuable mentoring has been provided also by Prof. Keijo Hämäläinen, who could be relied on to provide sound advice in every situation, from the best journal to publish your scientific papers in, to whether to hit the eight or nine iron from 120 meters, with the pin in the front of the green and a slight crosswind.

A key point in this thesis is the development of a combined x-ray scattering and microtomography setup. I was perhaps the chief architect of the implementation, but I cannot claim credit for the idea, which was conceived already before I started in the Department of Physics. In addition to the already mentioned professors, at least Dr. Marko Peura and the two laboratory engineers, Dr. Merja Blomberg and Phil.Lic. Pasi Lintunen deserve credit for not only that, but also for their seemingly never-ending patience in the face of my equally never-ending bombardment with technical questions of varying stupidity. Actually putting the equipment together was made possible with the expertise of the staff at the mechanics workshop, most prominently Ville Hänninen.

I will dearly miss the entire group of the x-ray lab, past and present: you have all been wonderful companions for this journey. Day in and day out, the lab has felt like a place where I am welcomed and where help was always available for scientific problems as well as taking my mind off research when needed. A special shout-out to the floorball and football crews, and Kari and subsequently Patrik for organizing them! On the scientific side, thanks especially to Inkeri, Ville and Paavo for all their

help with the scattering equipment.

Most of all, thanks to Aki: in a different context, our five-plus-some years of sharing a windowless basement with one other person as an office space might sound nightmarish, but in retrospect the humor, direct feedback on pressing concerns, and the occasional crazy stunt made sure I wouldn't have it any other way. There certainly were moments of frustration and annoyance as well, but the good memories, both in and out of our little cave, far outweigh the bad.

This thesis was not written in a vacuum, and would not have been possible without the understanding of my family and friends, who have supported me all through my studies, and reminded me that there is life outside of the lab as well. I am eternally grateful to Paulina, who stood by this endeavor almost the entire way, perhaps sacrificing the most while not experiencing first-hand the joy of discovery that makes science worth doing.

Grenoble, November 19th, 2014
*Jussi-Petteri Suuronen*

J.-P. Suuronen: Structural studies from nanoscale to macroscale with x-ray microtomography and microbeam scattering, University of Helsinki, 2014, 56 pages + appendices. University of Helsinki, Report Series in Physics HU-P-D223.

**Keywords:** x-ray scattering, x-ray microtomography, micrometeorites, anisotropic structures, nanostructure of clay materials, bentonite, clay-polymer composites, xylem embolism, tree physiology, steel-fiber reinforced concrete, fiber orientation

# Abstract

X-rays are an extremely versatile probe for materials characterization: while conventional medical x-ray imaging is used to visualize structures with macroscopic dimensions, x-ray diffraction and spectroscopy provide information on phenomena at atomic length scales. A fairly recently introduced intermediate-scale method is x-ray microtomography, which is used to image the internal structure of millimeter-sized samples at a resolution of approximately one micrometer. Especially in the case of hierarchical materials, a thorough description of the bulk properties depends on understanding the interplay of differently scaled effects. Multimodal studies characterizing material structures at different length scales are often crucial in achieving this goal.

In this thesis, x-ray diffraction, wide-angle x-ray scattering and microtomography were used to analyze the correlations between nanoscale and microscale structure, and microstructural features affecting macroscopic properties in representative model systems. A novel experimental setup was constructed that adds the capability for in situ x-ray scattering experiments to a state-of-the-art x-ray microtomography scanner. Using the microtomography reconstruction to target the x-ray beam in the scattering experiment enables mapping selected crystallographic properties with 200 micrometer resolution.

One of the first sets of samples analyzed with the new setup were a series of submillimeter-sized micrometeorites, whose volume and porosity are indicative of their atmospheric entry velocity. Using the combined setup, the microtomography results could be complemented by information on the micrometeorites' mineralogical composition and degree of crystallite orientation obtained with x-ray diffraction.

Consisting of stacked platelets with a high aspect ratio, clays and clay-based materials are prime examples of anisotropic materials, where the alignment of nanometer-thick particles produces discernible features also in the micrometer length scale. This was studied by combining microtomography with wide-angle scattering and transmission electron microscopy observations of clay-polystyrene nanocomposites with and without alignment of the clay particles by an external electric field. Compared with pure polystyrene, addition of small amounts of surface modified hectorite clay was found to

improve the thermal resilience without seriously degrading the mechanical properties.

Another clay material where the nanoscale orientation produces effect in a longer length scale is bentonite. Due to its exceptional swelling and water retention properties, compacted bentonite is used in many waste management applications, including its planned use as a buffer material in repositories for spent nuclear fuel. In this work, combining small-angle x-ray diffraction and microtomography with controlled humidity conditions allowed near simultaneous measurement of both the local clay platelet orientation and platelet spacing, as well as the orientation of microcracks developed in the drying sample. The anisotropic effects were found to be significantly weaker in natural bentonite compared with a purified montmorillonite sample.

Even with samples unsuitable for the associated scattering experiments, the three-dimensional information provided by microtomography can produce new insights into the microscopic features that influence the bulk properties of a material or biological system. In this work, a new three dimensional image analysis method was developed for quantifying the orientation distribution of steel fibers from tomography data of steel fiber reinforced concrete. As the orientation distribution plays a fundamental role in determining the bulk mechanical properties of the concrete, controlling the orientation is an open research question with significant economic importance. The results of the experiment showed a significant alignment of the fibers with the edge of the formwork and illustrated the utility of x-ray tomography for measuring the orientation distribution.

Water transport in trees is a second example where a phenomenon occurring over the length of the tree is easily disrupted by the development of micrometer-scaled embolisms within the xylem conduits. In this case, the utility of microtomography was demonstrated by non-destructively imaging the contents of individual xylem conduits within a living tree sapling under varying environmental conditions. This enabled following the same sample plants over an extended period of time, which has not been possible with conventional, destructive methods for measuring xylem embolism.

# List of papers

This thesis consists of an introductory part and six research articles, which are referred to by Roman numerals **I**–**VI** throughout the text.

**I** Mauroy, H., Plivelic, T.S., **Suuronen, J.-P.**, Hage, F.S., Fossum, J.O., and Knudsen, K.D. (2014). Anisotropic clay-polystyrene nanocomposites: synthesis, characterization and mechanical properties. *Applied Clay Science*, submitted.

**II** **Suuronen, J.-P.**, Kallonen, A., Hänninen, V., Blomberg, M., Hämäläinen, K., and Serimaa, R. (2014). Bench-top X-ray microtomography complemented with spatially localized X-ray scattering experiments. *Journal of Applied Crystallography* **47**:471-475

**III** Kohout,T., Kallonen, A., **Suuronen, J.-P.**, Rochette, P., Hutzler, A., Gattacceca, J., Badjukov, D.D., Skála, R., Böhmová, V., and Čuda, J. (2014). Density, porosity and internal structure of cosmic dust and alteration of its properties during high velocity atmospheric entry. *Meteoritics and Planetary Science* **49**(7):1157-1170

**IV** **Suuronen, J.-P.**, Matusewicz, M., Olin, M., and Serimaa, R. (2014). X-ray studies on the nano- and microscale anisotropy in compacted bentonite and calcium montmorillonite. *Applied Clay Science* **101**:401-408

**V** **Suuronen, J.-P.**, Peura, M., Fagerstedt, K., and Serimaa, R. (2013). Visualizing water-filled versus embolized status of xylem conduits by desktop x-ray microtomography. *Plant Methods* **9**:11

**VI** **Suuronen, J.-P.**, Kallonen, A., Eik, M., Puttonen, J., Serimaa, R., and Herrmann, H. (2013). Analysis of short fibres orientation in steel fibre reinforced concrete (SFRC) by X-ray microtomography. *Journal of Materials Science* **48**(3):1358-1367

# Author's contribution

In paper **I**, Jussi-Petteri Suuronen (J.-P.S.) planned and conducted the microtomography experiments, analyzed the tomography data and contributed to the discussion of results in the manuscript. In paper **II**, J.-P.S. was chiefly responsible for designing, organizing and carrying out the integration of the scattering system to the microtomography equipment, performed the example experiments and associated analysis, and wrote most of the manuscript. In paper **III**, J.-P.S. carried out the majority of the diffraction experiments and some microtomography experiments, was instrumental in the design of these experiments and their associated data analysis, and contributed to the methodology and analysis of the results in the manuscript. In papers **IV** and **V**, J.-P.S. designed and carried out the microtomography and scattering experiments and was the principal author of the manuscript. In paper **VI**, J.-P.S. participated in the design of the study and part of the experiments, designed and implemented the fiber separation algorithm, performed part of the data analysis, and contributed to writing the manuscript.

Paper **I** has been previously included in the dissertation of Henrik Mauroy (Institute for Energy Technology, Physics Department, Kjeller, Norway 2013), and paper **VI** in the dissertation of Marika Eik (Aalto University School of Engineering, Department of Civil and Structural Engineering, Espoo 2014).

# Other related work

Other publications by the author which are relevant for this thesis but not included in it:

- Penttilä, P., **Suuronen, J.-P.**, Kirjoranta, S., Peura, M., Jouppila, K., Tenkanen, M., and Serimaa, R. (2011). X-ray characterization of starch-based solid foams. *Journal of Materials Science* **46**(10):3470-3479

- Leppänen, K., Bjurhager, I., Peura, M., Kallonen, A., **Suuronen, J.-P.**, Penttilä P., Love, J., Fagerstedt, K., and Serimaa, R. (2011). X-ray scattering and microtomography study on the structural changes of never-dried silver birch, european and hybrid aspen during drying. *Holzforschung* **65**:865-873

- Kirjoranta, S., Solala, K., **Suuronen, J.-P.**, Penttilä, P., Peura, M., Serimaa, R, Tenkanen, M., and Jouppila, K. (2012). Effects of process variables and addition of polydextrose and whey protein isolate on the properties of barley extrudates. *International Journal of Food Science and Technology* **47**(6):1165-1175

- Svedström, K., Lucenius, J., Van den Bulcke, J., Van Loo, D., Immerzeel, P., **Suuronen, J.-P.**, Brabant, L., Van Acker, J., Saranpää, P., Fagerstedt, K., Mellerowicz, E. and Serimaa, R. (2012). Hierarchical structure and dynamics of juvenile hybrid aspen revealed using x-ray scattering and microtomography. *Trees – Structure and Function* **26**(6):1793-1804

- Salmi, A., Montonen, R., Salminen, L.I., **Suuronen, J.-P.**, Serimaa, R., and Hæggström, E. (2012). Cyclic impulsive compression loading along radial and tangential wood directions causes localized fatigue. *Journal of Applied Physics* **112**(12):124913

- Matusewicz, M., Liljeström, V., Pirkkalainen, K., **Suuronen, J.-P.**, Root, A., Muurinen, A., Serimaa, R., and Olin, M. (2013). Microstructural investigation of calcium montmorillonite. *Clay Minerals* **48**:267-276

- Penttilä, P., Kilpeläinen, P., Tolonen, L., **Suuronen, J.-P.**, Sixta, H., Willför, S., and Serimaa, R. (2013). Effects of pressurized hot water extraction on the nanoscale structure of birch sawdust. *Cellulose* **20**(5):2335-2347

- Mikkonen, K.S., Parikka, K., **Suuronen, J.-P.**, Ghafar, A., Serimaa, R., and Tenkanen, M. (2014). Enzymatic oxidation as a potential new route to produce polysaccharide aerogels. *RSC Advances* **4**:11884-11892

- Sayab, M., **Suuronen, J.-P.**, Hölttä, P., Lahtinen, R., and Kallonen, A. (2014). High resolution X-ray computed micro-tomography: a holistic approach to metamorphic fabric analyses. *Geology*, DOI: 10.1130/G36250.1. In press.

# Contents

# 1 Introduction and motivation

Considering that visualizing the internal structure of optically opaque objects was the very first application of x-rays, employed already by Röntgen himself (Röntgen, 1896), it is fascinating that in the past decade, x-ray *imaging* has again emerged as a 'novel' and 'growing' method of investigation in such diverse fields as plant physiology (Cochard et al., 2014), geosciences (Cnudde et al., 2006), or materials science (Buffiere et al., 2010; Maire, 2012). The major difference between present time and the 19th century lies, of course, in the scale and dimensionality of the investigation; in stark contrast to the millimeter-scale resolution in a two-dimensional image, achieved by Röntgen, modern synchrotron x-ray tomography setups can record three-dimensional images consisting of billions of voxels with micrometer resolution in a matter of seconds (Martin and Koch, 2006; Rack et al., 2010). More sophisticated contrast mechanisms, such as phase, diffraction, fluorescence or even chemical bond contrast (e.g. Stock, 2009, Ch. 4.8; Huotari et al., 2011; Ludwig et al., 2012; Martínez-Criado et al., 2012) also yield information which is fundamentally different from that given by familiar x-ray absorption imaging.

Compared with the traditional use as a medical diagnostic tool, for which x-ray computed tomography (CT) was originally developed (Hounsfield, 1973), scientific research with the method is often more computationally demanding: it is not enough to qualitatively assess the image for the existence (or lack thereof) of pathological features, but quantitative information needs to be extracted from the data by image processing techniques. Progress in the field is then driven by increasing computational power and new analysis algorithms, in addition to developments in x-ray production and detector technology. Luckily, the digital era has also brought about a wealth of research into digital image processing, and many concepts and algorithms are fairly straightforward to generalize into three dimensions. The required image analysis is also often similar across disciplines: while some fine-tuning may be needed, the basic building blocks of the data analysis algorithm (i.e. digital filters, morphological operations, segmentation and rendering routines) are the same regardless of whether the sample consists of wood, rock, or plastic.

As the resolution of x-ray microtomography (XMT) systems approaches the nanoscale, it is getting increasingly attractive to complement XMT results with the established methods for analyzing nanometer-sized structures. Multimodal studies combining XMT with x-ray scattering or fluorescence help link the observed microscale phenomena to the underlying nanometer-scale effects (Bare et al., 2014; Naik et al., 2006; Penttilä et al., 2013). In this thesis, the main focus will be on combining XMT data with x-ray diffraction (XRD) experiments. The benefits of such a combined experiment are accentuated if the data can be registered, i.e. the obtained diffraction patterns can be connected to specific features observed also in the microtomography

images (Stock, 2006). This is easily implemented in the diffraction tomography imaging technique (Johnson et al., 2008; Ludwig et al., 2012, 2008), if an absorption or phase tomogram is acquired simultaneously to the diffraction experiment, and also if a scattering tomography is performed by raster scanning the sample through a narrow beam at each projection angle (e.g. Bleuet et al., 2008; Schroer et al., 2006). The downside of this approach is that, until very recently, direct diffraction or scattering tomography has only been available at synchrotron radiation facilities. With most x-ray tube microtomography scanners, a separate instrument is necessary for the scattering experiment, and any spatial information on the scattering beam path within the sample is lost. To the author's knowledge, the first laboratory-scale (i.e. not on a synchrotron beamline) experimental setup for diffraction microtomography was presented by King et al. in 2013. The lack of so-called 'desktop', or 'bench-top' equipment is a serious hindrance on the path to make such experiments a routine method of investigation outside of cutting-edge research, as access to synchrotron facilities is limited. For most research groups, the need to apply for beamtime months ahead of the experiment also makes it less appealing to study riskier samples, on which it is not guaranteed that the method will provide significant results. For widespread application in research, and eventually routine use in industry or healthcare, it is therefore crucial that the state-of-the-art methodology developed at synchrotron facilities be adapted for use with x-ray tube systems, which are the economically feasible method of x-ray production for most individual institutions, companies or hospitals.

This thesis is organized around the topics described above, with an emphasis on method development rather than focusing on a specific field or type of material. In fact, the samples discussed illustrate the great variety of research topics in which these methods are applicable: paper **III** describes the effects of atmospheric entry on the internal structure of submillimeter-sized micrometeorites, while in paper **VI** the samples are 10 cm cores drilled from a full-sized floor slab of steel fiber reinforced concrete. Besides applicability to a wide range of different materials, one key advantage of x-ray tomography is non-destructivity: notwithstanding a small radiation dose, the experiment has no effect on the studied object beyond the manipulations necessary to mount the sample in the scanner. This enables scanning the same sample several times to observe changes in the microstructure over time, as was done in paper **V** to visualize the effects of prolonged drought on the water-conducting xylem of living birch saplings. The non-destructive nature of XMT scanning is also important when the samples are especially rare or valuable (as in paper **III**), and enables the in situ x-ray diffraction experiments presented in papers **II-IV**. When precise positioning of the scattering beam and exactly same ambient conditions are not important, the scattering experiment can of course be carried out using a dedicated instrument, as is the case in paper **I**. This article can be seen as a prelude to the remainder of the papers, illustrating how x-ray scattering experiments and microtomography yield complementary information

of the microstructure. Paper **II** then describes a novel, bench-top experimental setup that enables performing the two experiments in situ, which is utilized in paper **III** for the already mentioned micrometeorite study and in paper **IV** for analysing anisotropy in compacted bentonite clay. In papers **V** and **VI**, XMT without scattering experiments is applied to phenomena in a larger length scale. In the introductory part of the thesis, a description of the used experimental methods is followed by a short overview of each addressed research problem.

# 2 X-ray methods for materials characterization

## 2.1 Microtomography

### 2.1.1 Overview

A Finnish proverb says: "*A beloved child has many names*", which is especially true about x-ray microtomography. Since the introduction of the method in 1987 by Flannery et al., it has been called by different names and acronyms by different authors; perhaps the most common are micro-CT or µCT, which simply attach the prefix *micro* to differentiate from poorer-resolution medical CT. Other authors have chosen to emphasize the high resolution or contrast mechanism and x-ray production method with names such as "high-resolution x-ray computed tomography" (HRXCT or simply HRCT, e.g. Brodersen et al. 2013; DeVore et al. 2006) or even "synchrotron radiation phase-contrast X-ray tomographic microscopy" (srPCXTM, e.g. Derome et al. 2011; Trtik et al. 2007). In this thesis, the acronym XMT will be used as the most direct way to abbreviate X-ray MicroTomography (as used in the past by e.g. Fuloria and Lee 2009; Menon et al. 2011).

Regardless of the naming convention, the principle behind all these methods is the same: in the *acquisition* phase, digital 2D radiographs, termed *projections* in this context, are obtained from a multitude of directions spanning typically a 360° or 180° rotation. This is followed by tomographic *reconstruction*, where the information embedded in the projections is converted into a 3D grayscale volume consisting of a regular array of (typically cubic) *voxels*, the 3D analogue of pixels in a 2D digital image. The edge length of one cubic voxel is called the *voxel size* of the reconstruction. This workflow and operating principle are depicted in figure 1. In the basic case of absorption microtomography, which is typically the only available mode in x-ray tube based scanners (in contrast to synchrotron imaging beamlines), the voxel grayvalues reflect the linear attenuation coefficient $\mu$ of the sample. This parameter is related to the attenuation of the x-ray beam traversing the sample by Beer-Lambert's law

$$\frac{I}{I_0} = \exp(-\int_L \mu\left(\vec{r}, E\right) d\vec{r}), \tag{1}$$

where $I$ and $I_0$ are the attenuated and initial x-ray intensities, and $L$ is the path of the x-ray beam through the sample. An important thing to note is that $\mu$ is not determined solely by the sample, but is also a predominantly decreasing function of $E$, the energy of the incoming x-ray beam. When using a polychromatic ('white') source, such as an x-ray tube, this results in a phenomenon called *beam hardening*, or the mean energy of the transmitted x-rays shifting to higher energy with increasing penetration through the sample. Since the structure of the sample is a priori unknown, this shift cannot be completely taken into account, and results in beam hardening artifacts in

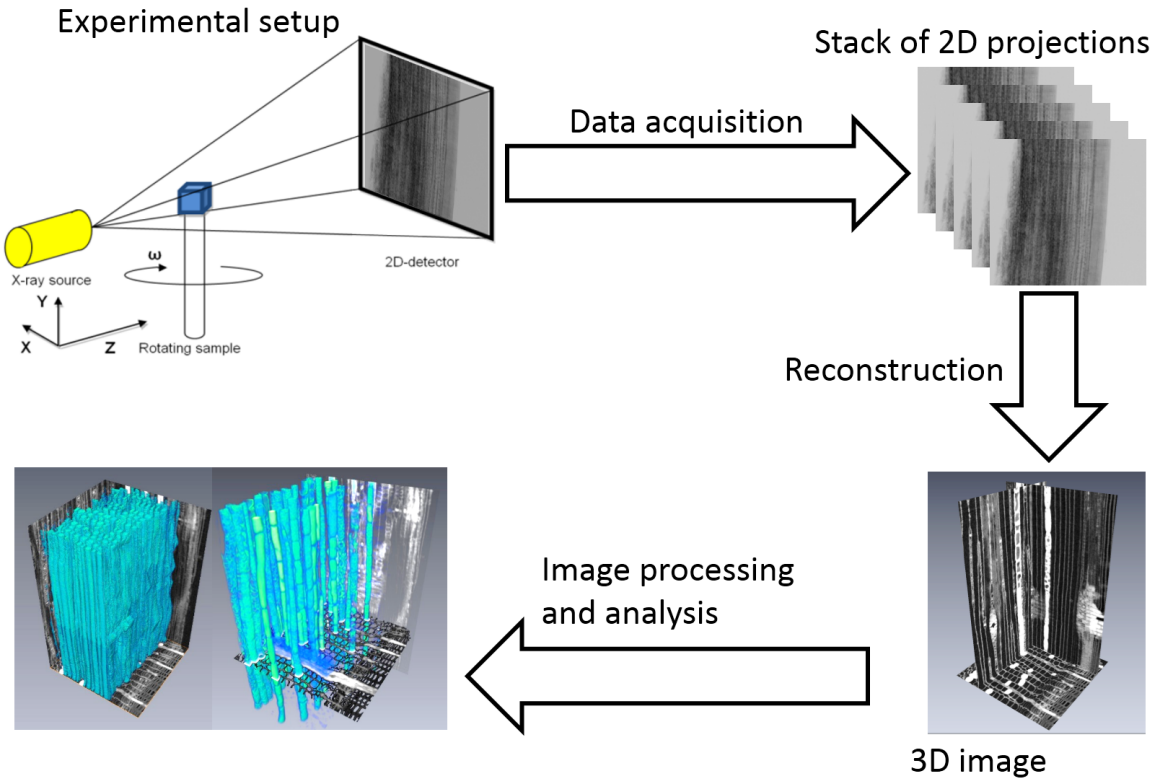


**Figure 1.** Operating principle and workflow of an XMT experiment. The sample shown in the images is Norway spruce (*Picea abies*) phloem stained with osmium tetroxide for contrast. At bottom left, the images show 3D renderings of sieve cell tissue (left) and phloem parenchyma (right) within the sample.

the reconstruction (see e.g. Barrett and Keat 2004; Buzug 2008, p. 425). With a monochromatic or quasi-monochromatic ('pink') x-ray beam, typically obtained from a synchrotron source, beam hardening can be ignored and equation 1 considered to accurately describe the measured intensity.

In addition to avoiding polychromaticity-related issues, the greater x-ray intensity, coherence and monochromaticity of synchrotron sources also facilitates the use of contrast mechanisms other than attenuation contrast. In particular, phase contrast imaging (e.g. Cloetens et al., 1999) allows visualization of refractive index variation within the sample, offering greatly increased sensitivity in the case of soft materials where attenuation contrast is low; a practical example of the difference can be found in e.g. (Mikkonen et al., 2014). Although most commonly in use at synchrotron facilities, the increased contrast with low-density materials and associated biomedical applications have sparked numerous studies aiming to enable phase contrast also with desktop systems (e.g. Mayo et al., 2003; Myers et al., 2007). However, as phase and fluorescence contrast have not been used in the papers included in this thesis, they will not be discussed further here, and the remainder of this section is devoted to the basics of

attenuation tomography. X-ray diffraction contrast tomography is addressed in section 3 and in paper **II**.

### 2.1.2 Reconstruction mathematics

The mathematical foundation for tomographic reconstruction was laid by Radon as early as in 1917[1], predating the first actual CT equipment by more than 50 years. Mathematically, little has changed with the downscaling of medical CT systems into microtomography equipment: the cone beam filtered back-projection (FBP) algorithm presented by Feldkamp et al. in 1984 is still a standard choice in most commercial XMT scanners. As the topic is covered in numerous textbooks on tomography (e.g. Banhart, 2008; Buzug, 2008), only the most basic case of a two-dimensional reconstruction in parallel-beam geometry is discussed here. The presentation follows loosely that given in (Kak and Slaney, 2001).

In the continuous case, a parallel-beam projection of a two-dimensional function $f(x, y)$ is given by its Radon transform

$$P_\theta(t) = \int_{-\infty}^{\infty} f(x, y)\delta(y\cos(\theta) - x\sin(\theta) - t)dxdy. \tag{2}$$

A key result behind tomographic reconstruction is the Fourier slice theorem (fig. 2), which states that the (one-dimensional) Fourier transform of the projection $P_\theta$ is equal to the two-dimensional Fourier transform of the original function along a line that is normal to the projection and passes through the origin. Mathematically, this can be written as

$$F_p(w, \theta) = S_\theta(w), \tag{3}$$

where

$$S_\theta(w) = \int_{-\infty}^{\infty} P_\theta(t)e^{-i2\pi wt}dt$$

is the Fourier transform of the projection and $F_p(w, \theta)$ is the polar coordinate presentation of the Fourier transform of the object function

$$F(u, v) = \int_{-\infty}^{\infty}\int_{-\infty}^{\infty} f(x, y)e^{-i2\pi(xu+yv)}dxdy.$$

The Fourier space variables $u, v$ and $w$ corresponding to the real-space coordinates $x, y$ and $t$ are termed *spatial frequencies*, analogously to signal processing terminology, where the Fourier transform is used to obtain the frequency composition of a time-dependent signal.

As noted by Radon, combining equations 2 and 3 implies that any suitably inte-

[1] see (Radon, 1986) for an English translation of the original paper

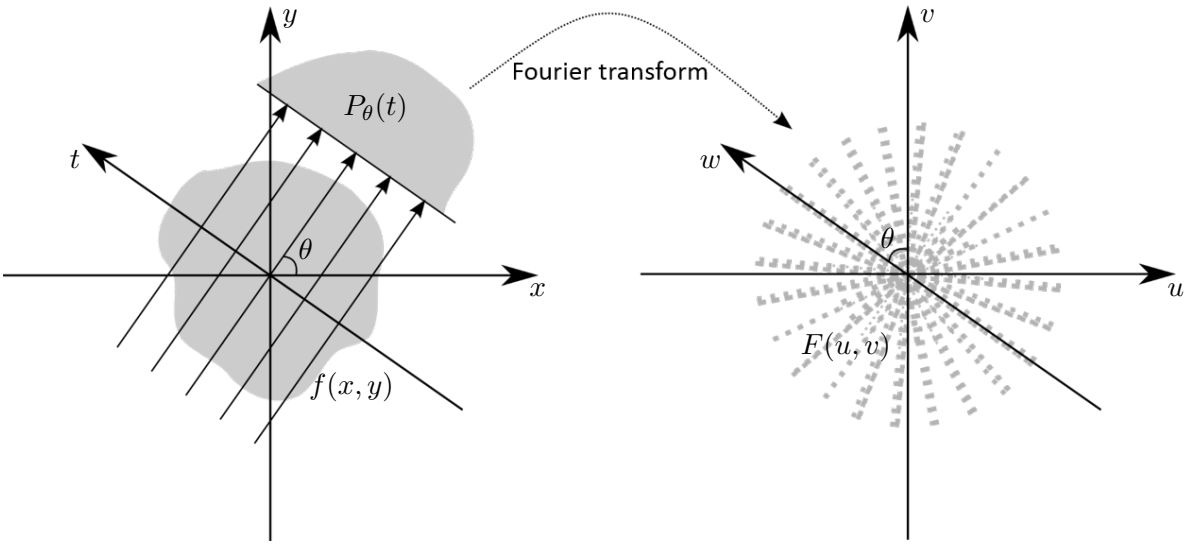


**Figure 2.** The Fourier slice theorem: the Fourier transform of the parallel projection $P_\theta(t)$ (left) is equal to the Fourier transform of the object function $f(x,y)$ along a radial line defined by $\theta$ (right).

grable and continuous function is uniquely defined by its projections $P_\theta(t)$, and could be obtained with the inverse Fourier transform

$$f(x,y) = \int_{-\infty}^{\infty}\int_{-\infty}^{\infty} F(u,v)e^{i2\pi(ux+vy)}dudv. \tag{4}$$

In a practical case, however, $P_\theta$ can only be measured at a limited number of angles, which results in an increasingly large interpolation error at high spatial frequencies. The filtered back-projection algorithm is obtained by performing a change of coordinates from the Cartesian $(u,v)$ to polar $(w,\theta)$. Substituting the relations

$$\begin{aligned} u &= -w\sin\theta \\ v &= w\cos\theta \\ dudv &= wdwd\theta \\ t &= y\cos(\theta) - x\sin(\theta) \end{aligned}$$

and equation 3 into equation 4 yields

$$\begin{aligned} f(x,y) &= \int_0^{2\pi}\int_0^{\infty} F_p(w,\theta)e^{i2\pi w(y\cos\theta - x\sin\theta)}wdwd\theta & (5)\\ &= \int_0^{\pi}\int_{-\infty}^{\infty} S_\theta(w)e^{i2\pi w(y\cos(\theta)-x\sin(\theta))}|w|dwd\theta & (6)\\ &= \int_0^{\pi}\int_{-\infty}^{\infty} |w|e^{i2\pi wt}\left[\int_{-\infty}^{\infty} P_\theta(t)e^{-i2\pi wt}dt\right]dwd\theta. & (7) \end{aligned}$$

In equation 7, the integrals over $w$ and $t$ represent a Fourier space filtering of the

measured projection by $|w|$, the so-called 'ramp' or 'Ram-Lak' [2] filter, whereas the outer integral is the back-projection part of the algorithm. For a practical implementation, equation 7 needs to be discretized, and the ideal ramp filter is often replaced with an alternative that suppresses the highest spatial frequency components, which are mostly associated with image noise. Some interpolation of the projection data is also necessary, as any practical detector will only measure the projection at discrete values of $t$. It is worth noting that equation 7 does not impose any restriction on the points $(x, y)$ at which the function is to be reconstructed. It is a practical choice, however, to choose a regular grid with a spacing corresponding to that between measured line integrals along the $t$ axis. A smaller spacing would simply increase the number of pixels in the image without improving the actual resolution, whereas a much larger spacing discards some information present in the projections.

The thus far presented case, where all line integrals in a single projection are parallel to each other, is generally only applicable at synchrotron radiation facilities. The brightness advantage allows making the source-to-detector distance so large that the x-ray beam can be considered planar, or obtaining different line integrals by raster scanning the sample through a highly focused or collimated beam in pencil beam geometry. In either case, a three dimensional reconstruction can be obtained by stacking individually reconstructed two-dimensional slices. A typical x-ray tube, on the other hand, is a point source whose comparably lower flux does not allow the collimation necessary to perform the scan in a reasonable time using pencil beam geometry. In the XMT system used in this thesis, the x-ray beam paths through the sample form a pyramid which has its apex at the x-ray tube exit window and base at the 2D detector (as in figure 1). Further changes are then required to equation 7 to account for the fact that the x-rays detected by an individual detector pixel pass through the sample at various heights (measured along the rotation axis) and for the loss of translational invariance in the projections (Feldkamp et al., 1984; Turbell, 2001). Cone beam geometry also requires acquiring projections over a full circle of rotation, since projections obtained from opposite sides of the sample are no longer the mirror image of each other. A distinct advantage of the cone beam geometry is that it enables geometric magnification: the useful voxel size of the reconstruction is the pixel size of the detector divided by the ratio of the source-to-sample distance to the source-to-detector distance. In parallel beam tomography, magnification is usually achieved by imaging the x-ray beam with a scintillator screen, and adding visible light magnifying optics between the scintillator and a visible light camera.

Although commonly used, inversion of the Radon transform by filtered back-projection is by no means the only possible method for tomographic reconstruction: alternatives include various algebraic reconstruction techniques which attempt to directly solve the linear system of billions of equations that describes the CT measurement

[2] Presented by Ramachandran and Lakshminarayanan (1971).

(Buzug, 2008, Ch. 6), and iterative methods (e.g. Siltanen and Mueller, 2012, Ch. 6) that use some kind of minimization scheme to reduce the error between the measured data and a forward-projected reconstruction. Suitably formulated, these alternative reconstruction methods can produce relatively good reconstructions with fewer projections than FBP, which is an important consideration if time resolution or radiation dose to the sample (or patient in medical imaging) is an issue. Unfortunately, they are also more computationally demanding than FBP, which has limited their applicability. Recent progress in using graphics processing units for accelerating tomographic reconstruction (Jang et al., 2009; Xu and Mueller, 2005), however, may yet enable these methods to overtake FBP as the reconstruction method of choice even with the largest microtomography datasets.

### 2.1.3 Image processing and tomography data analysis

Usually the most time-consuming part of a microtomography experiment, and almost certainly the one requiring the most input from the user is the analysis phase: converting the three-dimensional image that is the result of the reconstruction step into scientifically relevant information. While digital image processing in two dimensions has been around for decades, scientific equipment producing 3D data (such as XMT) has only become commonplace in the 21st century. The evolution of affordable and powerful imaging equipment has been accompanied by a rapid increase in data size. In a typical XMT experiment, the acquired volume is on the order of $2048^3$ voxels, which places a great demand also on the computational speed of algorithms.

In the easiest case, only a qualitative evaluation is needed and simply visualizing the data as two-dimensional images or a volume rendering is sufficient. More commonly, though, image processing is necessary to obtain quantitative parameters, which can then be compared between samples or with data obtained from the same sample using other methods. The methods used to this end differ from one type of sample to another, and comprise a research field on their own; this section does not attempt to describe them in detail, but rather to establish the terminology associated with manipulating volumetric data. The analysis approaches used in this thesis are discussed in section 4 and the included papers. More comprehensive works on digital image processing include those by Gonzalez and Woods (2002), Ohser and Schladitz (2009) and Banhart (2008, Ch. 3).

Figure 3 illustrates the various steps that may be necessary in order to arrive at the desired results. The example system is a small piece of Silver birch (*Betula pendula*) wood, in which the quantities of interest were the cross-sectional area of wood cell lumina and cell wall thickness.

The analysis often begins with *preprocessing* the data: the purpose of this step is to make the subsequent analysis easier by reducing noise or highlighting the features of interest. Digital filters are commonly used. In the example case, a bilateral filtering

(Tomasi and Manduchi, 1998) was used for denoising with minimal blurring of the data. The preprocessing may also include cropping unneeded sections of the dataset to speed up the analysis.

In this thesis, *binarization* refers to the division of the voxels in the image into two classes: those that represent the objects of interest, and those that do not. Another wording would be that the grayscale image is converted into a black-and-white image. The word binarization is used here, as most of the discussed samples are two-phase systems; if the sample consisted of more than one material of interest, the number of distinct values in the output of this step would naturally be more than two. Another word frequently used is *segmentation*, which is sometimes also considered to entail the subsequent step of identifying individual objects of the same material. The simplest way to binarize a grayscale image is to classify voxels based on their grayvalue in relation to a selected minimum and/or maximum threshold. In an image with good contrast, the image histogram has a peak corresponding to the material under investigation, and the thresholds can be set to the valleys on either side of the peak. A common occurence, however, is a histogram where the peaks corresponding to different materials overlap due to noise or artefacts in the image. Another reason for overlap is the partial volume effect, which is caused by features of the sample that are smaller than the voxel size of the reconstruction: a voxel's grayvalue then represents a volume-weighted average of the attenuation coefficients of the materials inside the voxel. The partial volume effect causes a zone of intermediate-valued voxels to appear at otherwise sharp boundaries between two differently attenuating materials in the data.

Simple thresholding can still yield acceptable results, especially if only differences between several analyzed samples are of interest, and the threshold can be selected in a pre-determined fashion in order to prevent the user from biasing the results. A classic automatic method for threshold selection is that presented by Otsu (1979). When simple grayvalue-based binarization is not possible, also the local surroundings of each voxel must be taken into account. In figure 3, a hysteresis method was used, which identified as cell walls all voxels with a high enough grayvalue, and all those connected voxels that lie in the 'fuzzy' grayvalue range between high and low grayvalues (representing the cell lumina). In the figure, the voxels classified as lumina are shown with a red overlay.

In some cases, the result of the binarization step is already the desired result from which the needed parameters can be quantified: an example would be a simple porosity calculation, where the quantity of interest would be the ratio between the number of pore pixels to total pixels in the data. If the properties of individual objects in the image need to be determined, further processing is necessary to assign all voxels in the material of interest to objects in a step called *labeling*. In general, one group of connected voxels is considered to form an object; in case physically distinct objects are connected in the image, a *separation* step is needed prior to assigning the labels. In

the example case, a combination of a morphological closing operation and watershed segmentation (Ohser and Schladitz, 2009, Ch. 4.3.3) were used to first separate cells that were connected in the binary data through errors in the binarization and open pits in the cell walls. The labeled cells are shown in colored overlay, along with the watershed lines (white) in figure 3.

After the labeling process, properties such as dimensions, volume, orientation or textural properties (in the original grayvalue image) can be measured for each label separately. In the example, the mean cross-sectional area of each cell has been been calculated according to the equation

$$D = \frac{V}{h\cos(\theta)},$$

where $V$ is the volume of the object (number of voxels in the object multiplied by the cube of the voxel size), $h$ is the height of the objects along the z-axis of the dataset, and $\theta$ is the angle between the object and the z-axis. The illustrations in figure 3 show a volume rendering of the dataset, where the cells have been colored according to $D$, and a histogram of the mean diameters of the *wood fibers* (excluding the larger diameter *vessel elements*).

Several commercial and open source software solutions exist for performing the above processing steps. In this thesis, Avizo Fire (Visualization Sciences Group /FEI, U.S.A) software and self-written MATLAB (The Mathworks Inc., U.S.A) codes were used to perform most of the image processing, along with VGStudioMAX (Volume Graphics, Germany) software for some of the visualizations. Popular freely downloadable or open-source alternatives to these include Blob3D (Mote et al., 2010) and Fiji (Schindelin et al., 2012).

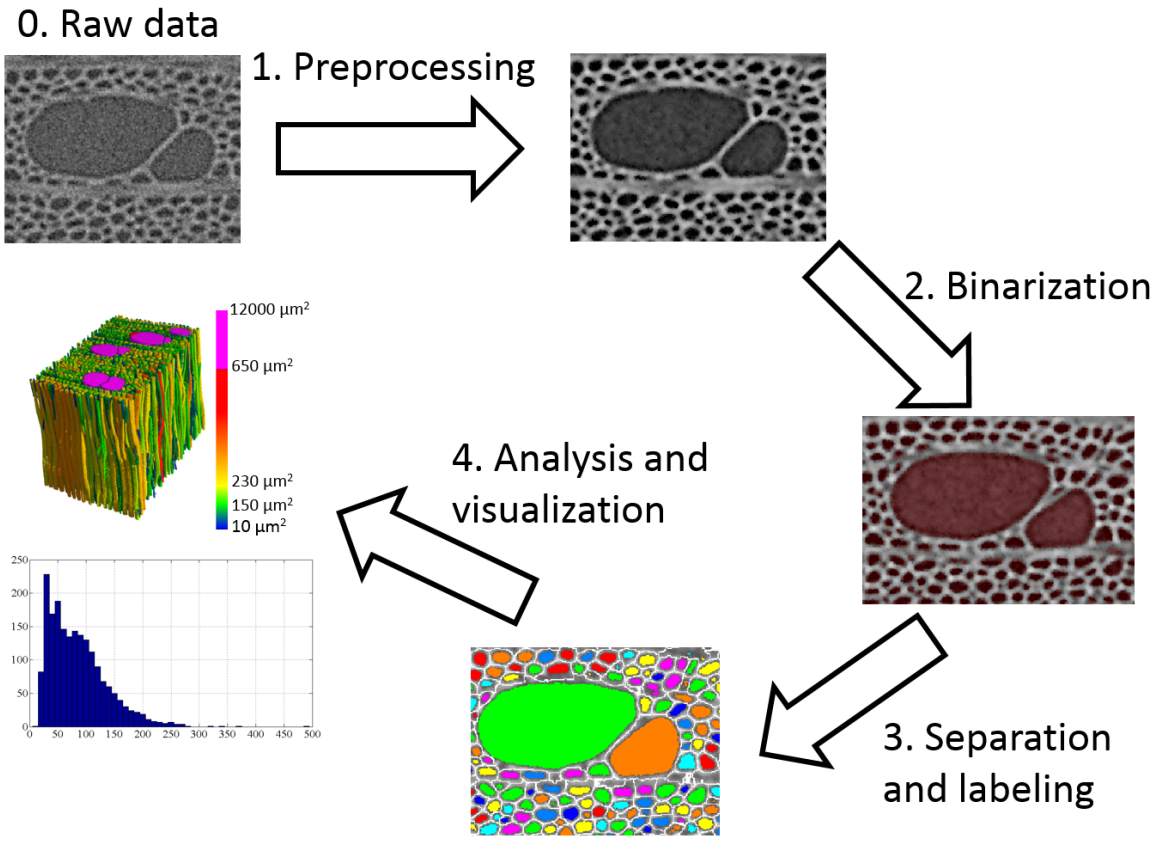


**Figure 3.** Workflow for analyzing the mean cross sectional diameter of wood fibers in a Silver birch sample imaged with XMT. See text for description of the processing steps.

## 2.2 X-ray scattering methods

For the purposes of attenuation imaging, the incoming radiation can be considered to be composed of individual particles, which are either removed from the beam by the sample or pass through the sample unhindered, contributing to the measured intensity $I$ in equation 1. Any coherently or incoherently *scattered* x-rays hitting the detector only serve to increase image noise, as the pixel they hit is more or less randomly selected. In x-ray scattering experiments, the coherently (i.e. with no change in the energy of the x-ray) scattered radiation is utilized to acquire information on periodic structures present in the sample. Such periodicities are formed, for example, by atoms in a crystal lattice (papers **II** and **III**), the lamellae in clay (papers **I** and **IV**, or cellulose microfibrils in a wood cell wall (Penttilä et al., 2013). For the purposes of this thesis, the scattering can be considered so weak that each x-ray is either transmitted through the sample, or coherently scattered exactly once. This assumption is called kinematical diffraction, as opposed to dynamical diffraction, which also takes into account multiple scattering phenomena.

### 2.2.1 X-ray diffraction theory

To understand how periodic structures give rise to a detectable signal in the scattered radiation, the x-rays should be considered as waves of electromagnetic radiation with wavelength

$$\lambda = \frac{hc}{E}, \tag{8}$$

where $E$ is the x-ray energy, $c$ is the speed of light and $h$ is Planck's constant ($\sim 6.6261 \times 10^{-34}$ m$^2$kg/s). Since the phase change of a coherently scattered wave is constant ($\pi/2$, Cullity and Stock 2001), a coherent beam scattered from two different targets undergoes constructive interference if the path difference between the scattered rays is an integer multiple of the wavelength. A textbook example of this is Bragg's law, used to describe diffraction from a crystalline solid

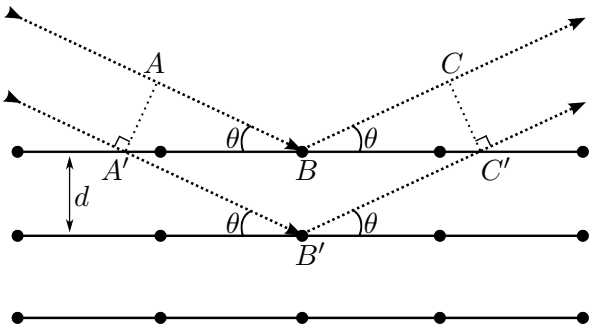


**Figure 4.** Bragg's law for diffraction: for x-rays of wavelength $\lambda$, a diffraction maximum is observed only at specific angles $\theta$, where the path difference between rays scattered from adjacent planes ($ABC$ vs. $A'B'C'$) is an integer multiple of the wavelength.

$$n\lambda = 2d \sin\theta. \tag{9}$$

In figure 4, $d$ is the distance between planes in a crystal lattice, i.e. a periodic array of lattice points, each of which has an identical basis of one or more atoms associated with

it. The scattering angle is defined as the angle between the incoming and outgoing x-rays, or $2\theta$. Diffraction peaks are observed at the exact angles, where equation 9 is satisfied. The integer $n$ is the order of diffraction: for the same lattice spacing, diffraction may happen at several different angles for different values of $n$. In this thesis, x-ray diffraction patterns are not presented as a function of the scattering angle, but the magnitude of the scattering vector

$$q = \frac{4\pi \sin\theta}{\lambda} = \frac{2\pi}{d} \tag{10}$$

is used instead, as it is only dependent on the corresponding lattice spacing and not on the wavelength. An added advantage is that diffraction peaks of different order are evenly spaced on the $q$-axis. The scattering vector is defined accordingly as the difference between the wavevectors of the incoming and outgoing radiation:

$$\vec{q} = \vec{k}_{in} - \vec{k}_{out}.$$

The scattering vector is related to an alternative way to formulate the diffraction condition. A crystal lattice is defined as set of points given by vectors of the form

$$\vec{r} = n_1\vec{a} + n_2\vec{b} + n_3\vec{c} \tag{11}$$

where $n_1$, $n_2$, and $n_3$ are integers and $\vec{a}$, $\vec{b}$, and $\vec{c}$ are linearly independent vectors that span the *unit cell* of the lattice. The reciprocal lattice is then given by the set of vectors

$$\vec{G}_{hkl} = 2\pi\left(h\frac{\vec{b}\times\vec{c}}{\vec{a}\cdot\vec{b}\times\vec{c}} + k\frac{\vec{c}\times\vec{a}}{\vec{a}\cdot\vec{b}\times\vec{c}} + l\frac{\vec{a}\times\vec{b}}{\vec{a}\cdot\vec{b}\times\vec{c}}\right) \tag{12}$$

where $h$,$k$, and $l$ are integers called the Miller indices associated with the reciprocal lattice point. An equivalent of Bragg's law is then the requirement that

$$\vec{q} = \vec{G}_{hkl}. \tag{13}$$

The geometry of the lattice thus defines the directions in which diffraction is observed from a crystal by a given x-ray beam. The diffraction peak that satisfies equation 13 for a particular set of indices $\{h, k, l\}$ is termed the $(hkl)$-*reflection* from the lattice. The intensities of the reflections are determined by the form factors and positions of the basis of atoms associated with each lattice point. An x-ray diffraction (XRD) or wide-angle x-ray scattering (WAXS) experiment consists of measuring the directions and intensities of the diffracted beams, and using this information to identify the crystal structure of an unknown sample or deduce structural parameters of a sample of known material.

### 2.2.2 Crystal size and orientation measurements

In an ideal, infinite crystal at absolute zero temperature, the scattered intensity is zero for any values of $\vec{q}$ that do not satisfy the diffraction condition. This is so because for every reflecting lattice plane, somewhere in the infinite crystal there exists another plane, which reflects x-rays of exactly opposite phase, resulting in destructive interference. In the practical case, the crystal is of a finite size, and some intensity is scattered also to directions not exactly equal to one of the 'allowed' values of $\vec{q}$. The width of the diffraction peak is therefore related to the size of the crystal along that particular crystallographic direction. Thermal fluctuations, impurities and dislocations in the crystal, as well as experimental effects, also serve to broaden the diffraction peaks.

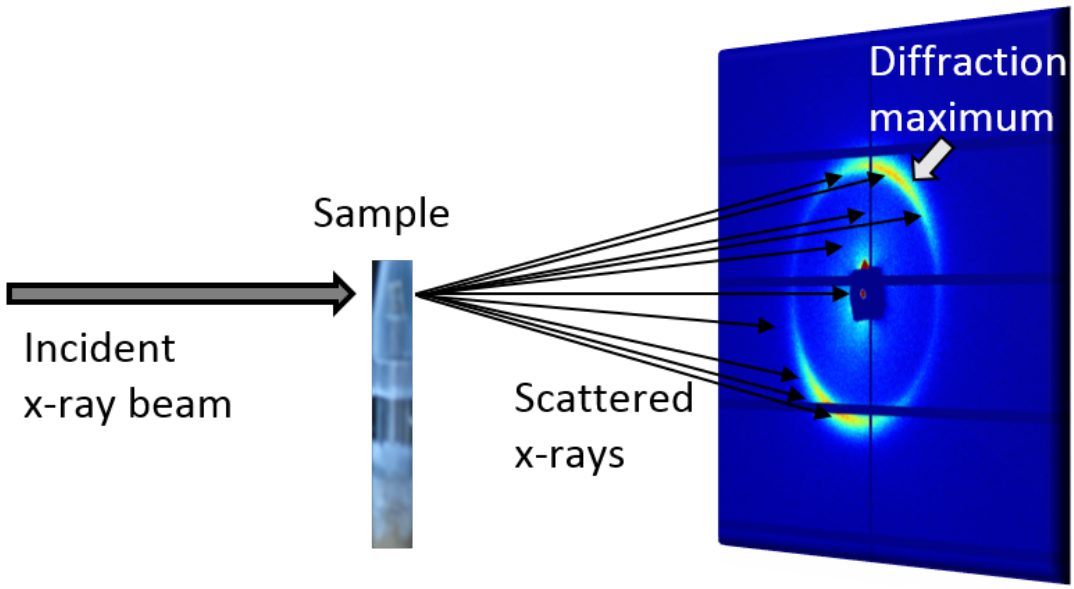


**Figure 5.** The measurement geometry for x-ray scattering experiments. X-rays strike the sample in a narrow, collimated beam, and the scattering pattern is recorded on an area detector perpendicular to the incoming radiation. In the center, the transmitted primary beam is partially blocked by the beamstop.

Diffraction will only occur at a certain scattering angle $2\theta$ if a suitably oriented crystal is present in the irradiated volume of the sample. As a result, measuring the complete scattering pattern of a single crystal involves rotating the sample through full $4\pi$ in solid angle at each measured $2\theta$ value, a task that requires significant mechanical complexity from the diffractometer. In powder diffraction, the task is made easier by grinding the sample as fine as possible before the measurement, so that a crystallite of every possible orientation can be assumed to be present. In this case, the scattering pattern is only recorded as a function of the absolute value of $q$, as any information regarding the crystal orientation is lost in the grinding. In this thesis, most of the samples are polycrystalline, and their *preferred orientation* in the undisturbed sample

is one of the quantities of interest in the experiment. This is also called the crystallographic *texture* of the sample. A large proportion of the reciprocal space is captured from a single exposure by utilizing a two dimensional detector in perpendicular transmission geometry, as illustrated in figure 5. In this geometry, the reflections from an ideal powder would be seen as rings of constant intensity on the planar detector, and preferred orientation is seen as intensity variations along the diffraction ring. The lattice spacing $d$ can be calculated from the distance of the ring from the transmitted primary beam (partially blocked by the beamstop) in the center of the detector.

XRD and WAXS are very useful methods for characterizing crystalline materials because the wavelength of x-rays commonly produced by an x-ray tube is of the same order of magnitude as the interatomic distances in many solids, about 1 Å = $10^{-10}$ m. To study larger structures, either the x-ray wavelength must be increased or the scattering angle made smaller. In the latter case, the method is called small-angle x-ray scattering (SAXS). In a SAXS experiment, typical parameters of interest are the shape, size and short-range ordering of scattering units in a length scale larger than the interatomic distances in crystalline solids. The data analysis associated specifically with SAXS is not treated further here, as it was not used in the papers included in this thesis. However, the combined XMT and scattering setup described in paper **II** and in the next section could, with some optimization, be used for SAXS experiments up to the 100 Å size range.

# 3 Microtomography with in situ scattering experiments

## 3.1 Multimodal studies with x-ray microtomography and scattering

As discussed in the previous chapter, x-ray scattering methods and XMT yield complementary information about the material structure at different length scales. Using both methods is therefore of interest in a variety of research problems; at the Department of Physics, University of Helsinki, especially wood samples have been the object of interest (Leppänen et al., 2011; Penttilä et al., 2013; Svedström et al., 2012), but also studies on e.g. Portland cement (Naik et al., 2006) and sea urchin teeth (Stock et al., 2002) can be found in the literature. Paper **I** of this thesis provides another example on the orientation and alignment of clay particles in clay-polystyrene composites.

In the wood experiments cited above, the objective was to characterize the bulk properties of the samples, and dedicated setups with a fairly wide ($\sim$ 1 mm) x-ray beam were used for the scattering experiments. With this approach, a fairly large volume of the sample is probed in single exposure of the detector, which not only improves the measurement statistics but also makes the results more representative of the bulk. The SAXS and WAXS results were then combined with quantitative or qualitative measurements on the entire XMT reconstruction. The reasoning behind constructing the combined XMT and scattering setup presented in paper **II** was to invert this approach: by using a microfocus x-ray source in situ with the existing XMT scanner, the scattering patterns could be linked to a specific sub-volume of the XMT reconstruction. This allows mapping the crystallographic properties of the sample with a resolution defined by the size of the scattering beam (typically $\sim$ 200 µm), and linking each scattering pattern with XMT analysis performed only on the subvolume probed by the scattering beam. Being able to localize the scattering experiment on a specific subvolume of the sample is a significant advantage if the sample is heterogeneous in the 100 µm size range. Alternatively, some structural parameter (particle orientation, composition etc.) may be changing from one part of the sample to another; in this case the same change can be observed in the µm length scale with XMT. In some cases, simply the saved trouble of not having to move the sample into a different environment for a dedicated scattering instrument is reason enough to utilize the combined system.

To the author's knowledge, the system constructed at University of Helsinki is among the first bench-top setups combining microtomography with x-ray diffraction at comparable resolution. An alternative approach would be that presented by King et al. (2013): mapping the grains in a polycrystalline metal sample is possible by collimating the beam from an XMT scanner to hit only the central part of the detector, and observing the paths of diffraction spots appearing on the detector outside of the

primary beam. Using synchrotron sources, diffraction tomography is possible both in the pencil beam geometry discussed in paper **II**, (Álvarez-Murga et al., 2012; Bleuet et al., 2008) and with full illumination of the sample (Johnson et al., 2008; Ludwig et al., 2008). Synchrotron radiation facilities naturally offer greatly reduced scan times and improved resolution, but bench-top systems have the potential to become a more accessible lower resolution alternative.

## 3.2 XMT/scattering setup at University of Helsinki

Figure 6 shows the combined microtomography and x-ray scattering equipment used in this thesis. As described in paper **II**, the setup is constructed around a Nanotom 180NF scanner (GE Measurement and Control Solutions, Germany) that has been custom-built inside an enlarged radiation protection enclosure to make room for the scattering equipment. Both systems are remotely controlled from the adjacent room. The scattering functionality is provided by a second x-ray tube (Incoatec GmbH, Germany) and area detector (Dectris Ltd., Switzerland), which are mounted at a 90° angle to the axis of the XMT beam. Molybdenum $K_\alpha$ radiation from the microfocus tube is focused and monochromated by the attached Montel optics to a rectangular beam. After the Montel optics, a variable divergence aperture allows fine-tuning the size of the focal spot, which is a tradeoff between spot size and intensity. A typical value for the beam size (length of the diagonal) is 200 µm. Closer to the sample, an additional vertical slit is used to remove from the beam those x-rays that have been reflected only once or not at all in the Montel optic. The range of $q$-values covered by the detector can be adjusted between $0.1 \ldots \sim 5\text{Å}^{-1}$ by adjusting the sample-to-detector distance.

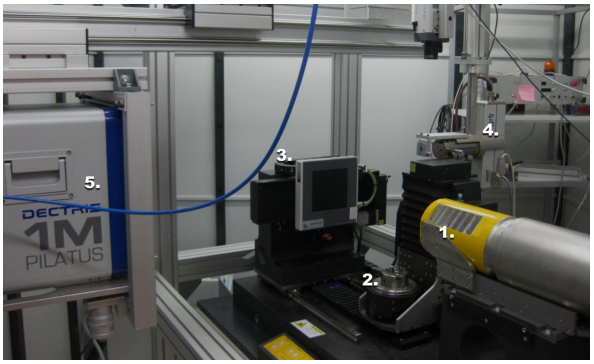


**Figure 6.** The combined XMT / scattering setup of papers **II**, **III** and **IV**. **1.** The nanofocus x-ray tube of the XMT scanner. **2.** The sample manipulator stage. **3.** CMOS (Complementary Metal Oxide Semiconductor) detector for XMT scans. **4.** Microfocus x-ray tube and focusing Montel optics for scattering experiments. **5.** Second area detector for collecting the scattering pattern.

After an XMT experiment, the CNC (Computerized Numerical Control) manipulator stage of the XMT scanner is re-positioned to place the desired subvolume of the sample in the scattering beam. The position of the scattering beam in the CNC coordinate system is known based on the calibration experiment depicted in figure 7: an XMT scan is acquired of a calibration phantom consisting of a small (approximately

the size of the scattering beam) particle of silver behenate (Huang et al., 1993) glued on a steel tip. The steel tip is easy to position in the scattering beam, as it completely blocks out the primary beam from the scattering pattern. After this, the exact coordinates of the scattering beam are straightforward to locate with the silver behenate, as it produces a very distinctive small-angle diffraction pattern on the detector. A larger silver behenate sample is also routinely used to calibrate the sample-to-detector distance for scattering experiments at low $q$-values. After the scattering beam has been located, the XMT experiments can be performed with the actual samples. It is then simple trigonometry to calculate the necessary CNC coordinates for selecting a specific path through the sample to be probed in the scattering experiment.

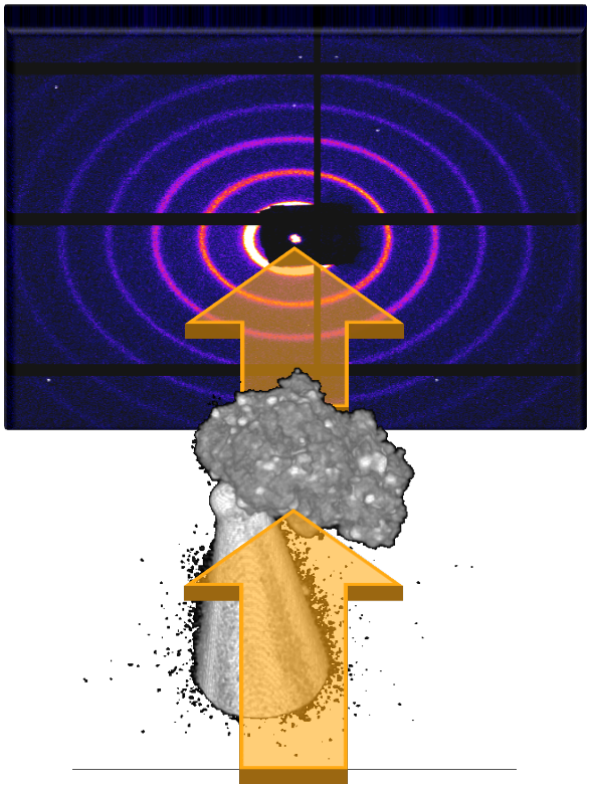

**Figure 7.** Calibration experiment to locate the scattering beam for combined XMT/scattering measurements: the location of a small silver behenate particle is known based on the XMT scan, and produces a very distinctive diffraction pattern when in the scattering beam.

It should be noted, that in the parallel-beam filtered back-projection formula (equation 7), the function $f(x, y)$ does not necessarily have to be the x-ray attenuation coefficient of equation (1), but any line-integrable property of the sample can be reconstructed from projection measurements. In pencil-beam x-ray diffraction tomography (XDT), the 'integration' in equation 2 is done by a single exposure of the detector, and the back-projected variable is some parameter (intensity of a certain reflection, crystallinity, etc.) calculated from the diffraction pattern. A one-dimensional projection is obtained by scanning the sample across the beam, after which the sample is rotated and the process repeated to acquire projections over a 180° dataset. For 3D imaging, the whole process needs to be repeated after shifting the sample in the vertical direction. This is called tomographic acquisition in pencil beam geometry, or sometimes 1st generation CT geometry, as it was in clinical use in the first medical CT scanners (Bushberg et al., 2002). Mathematically, it is simpler than the cone-beam geometry as a discrete version of equation 7 can be used directly for reconstruction. In paper **II**, a proof-of-concept XDT scan was carried out on a phantom consisting of two silver behenate

particles, using the intensity of the (001)-reflection as the projection variable. This experiment also served to validate the 200 µm resolution of the scattering experiments, as two particles of that diameter and spacing are resolved in the XDT reconstruction.

# 4 Studied systems and results

Sections 2 and 3 give an overview of the microtomography and associated x-ray scattering methods currently available at the Division of Materials Physics, University of Helsinki, where the research leading up to this thesis was conducted. The following section is devoted to the applications of those methods, illustrating the wide applicability of the technique and interdisciplinary nature of the work. The included papers span a variety of disciplines, including topics in planetary science, materials science, construction engineering and biology. Each of the topics is treated in a similar fashion: a brief general introduction to the problem is followed by an overview of the experiments and their results, focusing especially on what new information the methods discussed in this thesis bring to the subject. Specifics of the experimental procedure and detailed discussions of the implications of the results within the field are left to the respective papers and section 5.

## 4.1 Micrometeorites and interplanetary dust particles

### 4.1.1 Background

Along with remote telescopic observations and extremely expensive sample return missions, meteorites falling on Earth are a key source of information we have on the structure and composition of asteroids, which, in turn, provide insight to the structure and processes of the early solar system. Alongside its chemical composition, two fundamental physical properties to be determined are a meteorite's density and its porosity, defined by the equation

$$p = 1 - \frac{V_g}{V_b}, \tag{14}$$

where the *grain volume*, $V_g$, is the volume of the solid material in the meteorite, and *bulk volume*, $V_b$ is the total volume. Grain and bulk densities of the meteorite are calculated by dividing its mass with either the grain or bulk volume.

A key issue for determining both density and porosity is accurate determination of the sample volume, which may be a nontrivial task for typically irregularly shaped meteorite samples. Compared to terrestrial rocks, meteorites are rare and should preferentially be studied with nondestructive and noncontaminating methods. In the case of larger meteorites this is not an insurmountable problem, with helium pycnometry and the so-called Archimedean glass bead method being prominent noninvasive methods for grain and bulk volume determination (Consolmagno et al., 2008). However, much of the extraterrestrial material deposited on the Earth is in the form of smaller particles. Micrometeorites and interplanetary dust particles are not only indicative of the composition of asteroid surface material, but can also be deposited from comets and from interstellar sources (Nesvorný et al., 2010, 2006). As the precision of He pycnometry

is typically of the order of 20 $mm^3$ (Consolmagno et al., 2008), and the glass bead method is limited to approximately 5 $cm^3$ (Macke et al., 2010), these methods can not be used on very small small samples. The glass bead method can be replaced by the more laborious 3D visible light laser imaging (McCausland et al., 2011), but even that is insufficient to study micrometeorites, which are typically less than one millimeter in diameter.

X-ray microtomography provides a solution to the problem of accurate volume determination of micrometeorites and also allows simultaneous measurement of the porosity, down to the resolution of the instrument. Furthermore, grain volume measurement with XMT takes into account possible closed porosities within the sample, which would be unaccessible in He pycnometry. Additionally, the obtained volumetric image can be used to analyze the internal and surface texture. However, while the structure of larger meteorites has been imaged with tomographic methods for over 15 years (Friedrich et al., 2008; Hezel et al., 2013; Kondo et al., 1997), there have been only a few systematic studies of micrometeorites (e.g. Taylor et al., 2011). One interesting example is the combined x-ray diffraction and microtomography study on cometary dust by Nakamura et al. (2008).

### 4.1.2 Aim and key results of the experiment

In paper **III**, we conducted a similar study as Nakamura et al. (2008), on a series micrometeorites collected from the Atacama desert in Chile and Novaya Zemlya archipelago in northern Russia. Using the combined setup of paper **II**, we performed a textural classification and volume measurements with XMT, followed by an analysis of the crystal structure and preferred orientation of most of the samples with XRD measurements. A specific aim was to analyze the evolution of the meteorite's internal structure during its entry through the atmosphere. Since every meteorite recovered on Earth is subject to these changes, accurate modeling of the atmospheric entry is crucial for any interpretations one might make of the parent bodies based on meteorite material.

The sample set consisted of a total of 32 micrometeorites, of which 24 were completely melted, 3 partially melted and 5 unmelted, according to the classification by Genge et al. (2008). A cross-sectional slice and a volume rendering of each type is presented in figure 8. The melted micrometeorites were further divided into glassy, barred olivine and porphyritic olivine subtypes, whereas partially melted samples were of a scoriaceous subtype, and the unmelted micrometeorites, with one exception, were fine grained. The microtomography experiment also revealed inclusions within some of the melted meteorites, three of which possibly consist of relict material that survived the atmospheric entry without melting. One melted micrometeorite had a large metal inclusion. While the XRD patterns revealed all studied micrometeorites to be of a primarily olivine composition, there was significant variation in the degree of preferred orientation observed in the melted micrometeorites: the barred olivine subtype showed

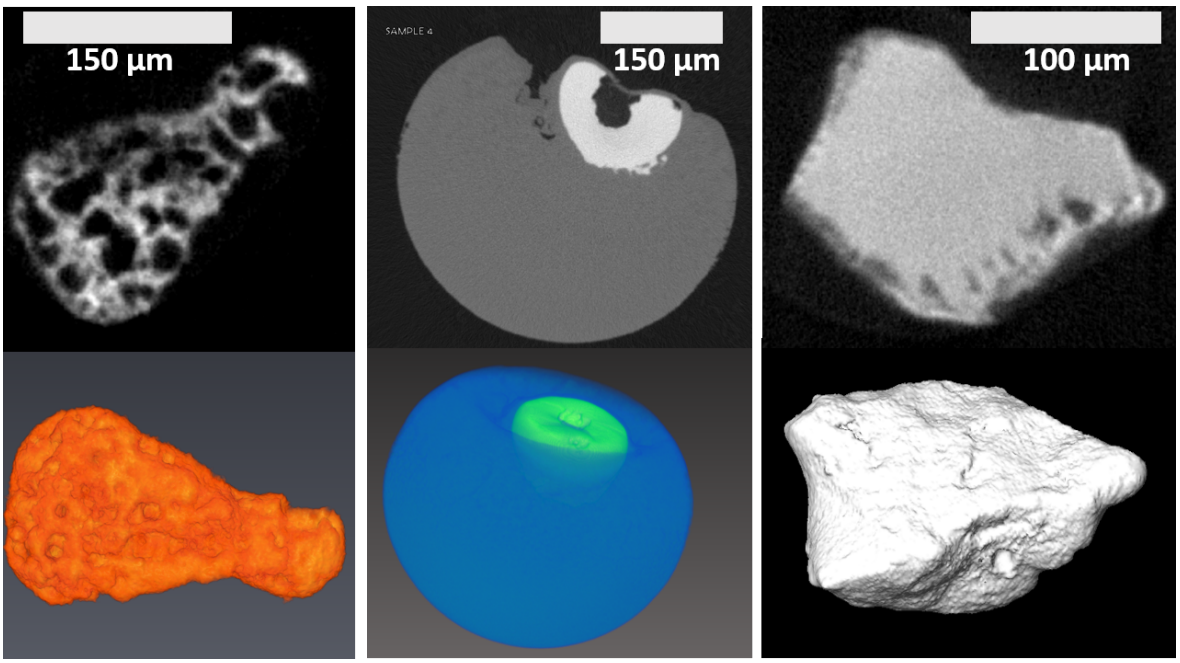


**Figure 8.** Cross-sectional images (top) and volume renderings (bottom) of a partially melted (left), completely melted (center) and unmelted (right) micrometeorite. The completely melted micrometeorite has a metal inclusion.

primarily strong preferred orientation, whereas the glassy subtype was mostly not oriented. Of the remaining types, only two samples were analyzed with XRD, which prevents any definite conlusions.

The advantage of the combined XMT/XRD system was that the diffracting beam could be aimed either hitting or missing the relict inclusions, which were all found to contain very well-oriented material, even in the otherwise randomly oriented glassy micrometeorite. Unfortunately, the scattering from the inclusion was fairly weak, and only produced two discernible peaks in the overall scattering pattern. This made it impossible to identify the mineral without obtaining an excessive amount of additional diffraction patterns. The main conclusions regarding what happens to the micrometeorite during atmospheric entry can be drawn from the porosity data, which shows greatest porosity (16-25 %) in the partially melted micrometeorites. On the other hand, the unmelted micrometeorites were more porous than the completely melted samples. One outlier unmelted micrometeorite had a very fragmental structure and a porosity of over 50 %. The XMT data thus supports the view that the relationship between micrometeorite porosity and atmospheric entry velocity is not linear. Instead, meteorites arriving at a relatively low velocity remain in their pristine state, and intermediate entry velocity results in heating that is enough to evaporate some volatile compounds, but insufficient to completely cause homogenization of the meteoroid. Complete melting is then accompanied by a loss of porosity and the meteoroid assuming a more or

less spherical droplet shape.

## 4.2 Structure of smectite clays

Clays possess an interesting microstructure, consisting of very thin ($\sim 10$ Å), but relatively wide (up to $\sim$ 1 µm) platelets stacked on top of each other. In this thesis, a clay particle consisting of several stacked platelets is termed a *tactoid*. All clays studied in this thesis either belong to, or are structurally very similar to a group of clay minerals known as smectites. In smectites, one platelet consists of three layers of cations coordinated with oxygen: one octahedrally coordinated layer ($Al^{3+}$, $Fe^{3+}$, $Cr^{3+}$, $Mg^{2+}$, $Zn^{2+}$ or $Li^{+}$) sandwiched between two tetrahedrally coordinated layers of $Si^{4+}$ or $Al^{3+}$ (Brigatti et al., 2013). In smectites, this platelet carries a negative charge due to the presence of lower valence cations instead of $Al^{3+}$ in the octahedral sites or instead of $Si^{4+}$ in the tetrahedral sites. This negative charge is balanced by *interlayer cations* (typically ions of the alkali or alkaline earth metals) present in the space between platelets; the remainder of the interlayer space is filled by one or more layers of water molecules hydrating the cations. The crystal structure of the most commonly used smectite, montmorillonite, is shown in figure 9, according to a structural simulation model by Viani et al. (2002). Especially the basal spacing of the unit cell is only an estimate, as the actual spacing will vary according to the hydration state of the clay.

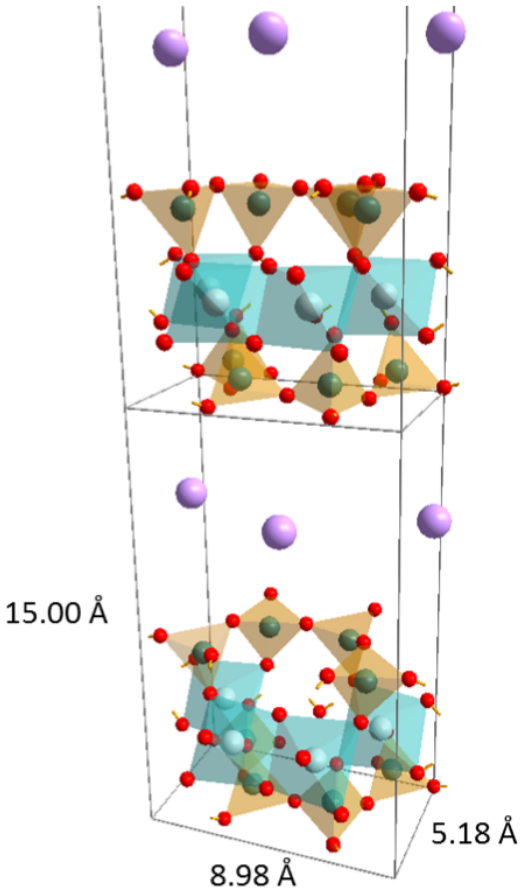


**Figure 9.** The crystal structure of calcium montmorillonite, showing how a layer of octahedrally coordinated $Al^{3+}$ (white) and two tetrahedrally coordinated layers of $Si^{4+}$ (green) form a clay platelet. The oxygen is shown in red, and interlayer $Ca^{2+}$ between platelets in purple. Water surrounding the interlayer cations is not shown. In the actual structure, also some substitutions of lower valence cations for the displayed $Si^{4+}$ or $Al^{3+}$ will occur.

Smectites are expandable clays: not only water, but also other molecules may enter the interlayer space, causing the distance between platelets to grow and the clay tactoid

to swell. Following the nomenclature in Bergaya and Lagaly (2013), this process is called *intercalation*, and such a swollen clay is said to be *delaminated*. The distance between platelets is then a complex function of the type of the interlayer cation (often given with the mineral name) and the humidity, temperature and chemical environment of the clay. It should be noted that the number of platelets making up a tactoid also varies: in some conditions, the platelets may become completely separated from each other, or *exfoliated*. An important property explored in this thesis is that the number of platelets in a tactoid is normally less than one hundred even under optimal conditions. Tactoids thus have a very high aspect ratio, and clays are very anisotropic materials when well oriented.

## 4.3 Clay-polystyrene nanocomposites

### 4.3.1 Background

The readiness of smectites to delaminate and accept other molecules in the interlayer space allows many possibilities for surface modification of clays. An industrially important example is the introduction of organic molecules into the interlayer space, producing organoclays (de Paiva et al., 2008). This can happen via several routes, for example various electrical interactions between a neutral organic molecule and the clay platelets, replacing the inorganic interlayer cations with organic cations, or displacing the interlayer water by intercalated organic anions (Lagaly et al., 2013). In addition to their use as e.g. rheological (Jones, 1983) or fire-resistant (Gardelle et al., 2013) additives in paints and coatings, or catalysts in biodiesel production (Ghiaci et al., 2011), smectite organoclays can also be used to create clay-polymer nanocomposites (CPNs, Lagaly et al. 2013). In CPNs, the properties of the pristine polymer are altered by intercalation of the polymer into clay tactoids (intercalated CPNs), or by the dispersion of the exfoliated clay platelets in the polymer matrix (exfoliated CPNs). If clay tactoids are dispersed in the matrix without intercalation or exfoliation, the material is termed a microcomposite (Bergaya and Lagaly, 2013). Although difficult to achieve, total exfoliation of the clay is generally considered to result in greater improvement of the polymer properties (Gopakumar et al., 2002; Paul and Robeson, 2008). Incorporation of the highly anisotropic smectite clay particles has been observed to improve e.g. the mechanical or thermal properties of the polymer even at fairly low weight fractions ($< 10\%$) of the clay (Paul and Robeson, 2008; Siengchin et al., 2007).

### 4.3.2 Aim and key results of the experiment

The great variation of available polymers and possible surfactants have led to an abundance of studies into the effect of various smectite additives on polymers (see Lambert and Bergaya 2013 for an overview). Most of the literature is concerned with

improving the bulk properties of polymers, but especially in the case of mechanical properties, many applications require strength along a specified direction in the final structure. The traditional way of producing anisotropy in a composite material is the use of fibers, which tend to have macroscopic dimensions. In paper **I**, nano- and microscale anisotropy was induced into polystyrene-organoclay nanocomposites through the application of an electric field. Organoclays were produced by exchanging the interlayer cations of two smectite clays (Na-montmorillonite and hectorite) and two synthetic clays (laponite and lithium-fluorohectorite) with the ammonium ion from cetyltrimethylammonium (CTAB), and oriented by applying a 625 V/mm alternating electric field during in situ polymerization of polystyrene. As the initial hypothesis, the electric field would cause polarization of the clay tactoids along the platelets, which would then orient in fiber-like chains with the stacking direction perpendicular to the electric field.

In addition to mechanical testing to detect anisotropy of the mechanical properties and thermogravimetric analysis to measure their thermal resilience, x-ray scattering and microtomography were instrumental in characterizing the formed structures: synchrotron-based WAXS of the (001)-reflection was used to verify the desired tactoid orientation and to determine tactoid size along the stacking direction. XMT, on the other hand, provided 3D visualizations of the aggregation of clay particles and chain formation in the microscale. The x-ray observations were complemented with transmission electron microscopy (TEM) imaging and optical microscopy.

The XMT results revealed interesting differences in the agglomeration of different clays: both synthetic clays seemed to aggregate into larger particles than the natural smectites, while easily visualized chains were only formed in the laponite composite. Analysis of the (001)-reflection with WAXS, on the other hand, revealed all electric field aligned samples to have intended tactoid orientation with the stacking direction perpendicular to the electric field indicating that none of the clays were completely exfoliated, which would result in disappearance of the reflection. Curiously, the tactoid size was smallest in the laponite composite, which nevertheless showed more prominent aggregation of particles in XMT. Unfortunately, the mechanical properties of the composites proved to be inferior to pure polystyrene under compression tests, with hectorite and laponite composites having yield strength, compressive modulus and fracture toughness similar to pure polystyrene, and montmorillonite and fluorohectorite giving significantly reduced values. The electric field laponite composites, however, showed noticeable anisotropy in the mechanical properties, which is likely linked to observed formation of clay particle chains. Moreover, all of the composites showed improved thermal resilience over pure polystyrene: this leads to the conclusion that CTAB-modified hectorite is the most promising additive of the studied clays, improving the thermal resilience without overly degrading the mechanical properties.

## 4.4 Bentonite and purified montmorillonite clay

### 4.4.1 Background

The swelling ability of smectites, especially montmorillonite, is extensively used in waste disposal applications, where clay liners are used to prevent the spread of contaminants into the environment from landfills and polluted land sites (Wagner, 2013). Smectites are particularly attractive liner materials, as their ability to absorb water limits the transport of contaminants by advection, and the high surface area allows for retardation of contaminants through adsorption on the platelet surfaces. Typically the clay used for this purpose is bentonite, which is a mixture of montmorillonite clay and various non-clay minerals such as quartz, feldspars or calcite. One exceptionally demanding use for clays in waste management applications is in the geological disposal of used nuclear fuel. The high radioactivity and long half-lives of many radionuclides produced in fission power reactors require that the spent fuel elements be isolated from the biosphere for very long times: one proposed figure for the relevant time scale is one million years (Dohrmann et al., 2013). Clay materials are involved in these designs in two ways; repositories in e.g. Finland and Sweden are designed to incorporate an engineered barrier of compacted bentonite (Posiva, 2012; SKB, 2011), while French and Swiss designs rely on natural clayrock formations as release barriers in addition to bentonite (Andra, 2013; Nagra, 2002). In the KBS-3 concept utilized by SKB and Posiva, the compacted bentonite buffer has three safety functions: it is intended to isolate the copper canister containing the fuel from the environment, to be ductile enough to provide mechanical protection for the canister, and to act as an independent release barrier in the event of canister failure (Juvankoski, 2013). The swelling, transport and mechanical properties of compacted bentonites and natural clayrock formations are therefore integral components of safe disposal of spent nuclear fuel.

One sometimes overlooked aspect with potentially significant implications to the functioning of a spent nuclear fuel repository is the anisotropy of the clay particles, which can translate into anisotropic bulk properties if the clay barrier exhibits significant preferred orientation. Such preferred orientation is often present in natural clayrock and shale formations, where the clay minerals tend to sediment along specific bedding planes, and clay tactoid and porosity orientation in these systems has been the subject of multiple studies (e.g. Keller et al., 2011; Wenk et al., 2008). In engineered barriers, preferred orientation may result from the treatment of the clay: uniaxial compaction could result in tactoids aligning with the stacking direction parallel to the axis of compaction. Some anisotropic effects have already been reported in the diffusion coefficients of compacted bentonite samples (Sato and Suzuki, 2003; Suzuki et al., 2004), but few authors assess the produced anisotropy at the micro- and nanostructural level.

### 4.4.2 Aim and key results of the experiment

In paper **IV**, the structural anisotropy in compacted bentonite was characterized with the combined XMT and x-ray scattering setup under varying humidity conditions. The samples consisted of MX-80 bentonite and purified calcium montmorillonite, which were first saturated with water or 0.1 M perchlorate solution in a confined sample cell to simulate the conditions in the final nuclear fuel repository. After initial measurements in the saturated state, the relative humidity surrounding the samples was lowered, and the formation of desiccation microcracks within the sample was observed with XMT. The XMT results were linked to the local evolution of the nanoscale structure based on small-angle x-ray diffraction measurements. The emphasis was on quantitative evaluation on orientation effects on the clay, with the tactoid orientation measured by azimuthal integration of the (001)-reflection of montmorillonite, and compared with the orientation of microcracks in the part of the sample intersected by the diffracting beam. The microcrack orientation was measured through first binarizing, and then calculating the sum of 2D autocorrelations of the pore volume sampled by the diffraction experiment. The direction where this summed autocorrelation descends most rapidly was then selected as the direction that was on average perpendicular to the microcracks. For both methods, a similar measure for the degree of preferred orientation was also devised, evaluating the azimuthal intensity variation of the (001)-reflection for diffraction data, and the anisotropy of the summed autocorrelation image for XMT data.

The results show a clear difference between the two clay types, with Ca-montmorillonite being well-oriented when observed with either method, and MX-80 appearing very isotropic. Furthermore, the orientation of microcracks in the purified and ion-exchanged Ca-montmorillonite correlates well with the tactoid orientation, indicating that the desiccation microcracks tend to appear along the long rather than short edge of tactoids. This difference can be attributed to two factors. Firstly, the non-clay accessory minerals present in the MX-80 sample are essentially incompressible at the pressures used for compaction, and cause a distortion to the stress field which prevents the compaction from aligning the clay particles. Secondly, the purification process of the Ca-montmorillonite involves sedimentation of the purified clay, which is likely to result in better-oriented grains already before compaction. Analysis of the scattering intensity versus $q$-value (equation 10) revealed that the number of water layers in the interlayer space was not constant for a fixed relative humidity, but peaks corresponding to mixtures of hydration states were observed. This drying behaviour was similar to previously observed swelling heterogeneity (Devineau et al., 2006; Ferrage et al., 2005).

A dependence of diffusion and structural anisotropy on the purity of the clay was already described earlier by Sato and Suzuki (2003), who noted that bentonite with only 50 % smectite was much more isotropic than nearly pure montmorillonite. Their

proposed microstructural model seems well supported by the results of paper **IV**. In the context of spent nuclear fuel disposal, the anisotropy present in bentonites with very high smectite content is a factor to be taken into account or exploited in the design of the buffer, and certainly needs to be considered when modeling bentonite properties based on experimental data obtained using pure montmorillonite.

## 4.5 Xylem embolism

### 4.5.1 Background

Upward transport of water from the soil to transpiring leaves is a fundamental process in the physiology of terrestrial plants. In trees, this uptake takes place over a distance of tens of meters, and, according to the cohesion-tension model of transport (Cruiziat and Richter, 2006), is due almost entirely to physical processes: the water forms a hydraulically continuous network of narrow liquid columns from the roots to leaves, and flow is driven by the pressure drop associated with transpiration in the leaves. As a consequence, the water in the conducting xylem is under tension (negative pressure) and susceptible to cavitation, or the formation of gas bubbles in the water column. Under negative pressure these bubbles can expand to fill an entire conduit, creating an embolism which blocks the water flow.

The ability of trees to withstand embolisms has an important impact on their tolerance of drought conditions (Ogasa et al., 2014; Pinto et al., 2012), an issue of increasing importance as global warming causes increasing fluctuations in the precipitation conditions of many forests (Allen et al., 2010; Auclair, 1993). Besides drought, also freeze-thaw cycles experienced by temperate and boreal species are known to cause embolism formation (Sperry et al., 1994; Taiz and Zeiger, 2010). Some tree species have also been found to be able to refill embolized conduits with water. Well-known methods of refilling are the buildup of positive root pressure by active loading of solutes into the roots and elevated stem pressures during spring thaw (Sperry et al., 1994; Wheeler and Holbrook, 2007). A more controversial method is so-called active refilling, which is thought to occur while the plant is transpiring, and the xylem as a whole is under tension. This implies hydraulic isolation of the refilling vessel from the surrounding conduits (Holbrook and Zwieniecki, 1999).

Studying the cavitation resistance and refilling capability of trees and other woody plants has been complicated by the lack of methods suitable for observing the phenomenon in live plants. Traditional methods have included measuring the percentage loss of hydraulic conductivity (PLC) of excised stems (e.g. Choat et al., 2010; Ogasa et al., 2010; Salleo et al., 2004), introducing a dye into the transpiration stream and observing its spread in sectioned samples with a microscope (Sano et al., 2005), and cryo-electron microscopy of samples frozen with liquid nitrogen (Utsumi and Sano, 2007). Being destructive, none of these methods allow monitoring the same sample over an extended

period of time, and conclusions must be drawn from analysis of anatomically similar samples harvested at different times. Moreover, the microscopy techniques are relatively laborious and prone to artifacts which may interfere with the interpretation of the results (Canny and Huang, 2001; Cochard et al., 2001), and also the validity of many PLC measurements has recently been called into question (Sperry, 2013).

These issues highlight the need for nondestructive methods able to directly visualize the water contents of individual cells within an intact plant. The ability of XMT to achieve precisely that was first shown by Brodersen et al. (2010) using synchrotron radiation, with a significant improvement in resolution over magnetic resonance imaging (Choat et al., 2010; Holbrook et al., 2001), which is only able to resolve the large vessel cells.

### 4.5.2 Aim and key results of the experiment

The objective of paper **V** was to explore the possibility of using a bench-top XMT system for visualizing cavitation and potential embolism repair in living tree saplings. As x-ray tube-based systems are significantly more common than suitable synchrotron beamlines, this could lead to easier adoption of the technique by the plant physiological community. The experiments were carried out on two broadleaved (angiosperm) trees native to Finland, Silver birch (*Betula pendula*) and Curly birch (*B. pendula* var. *carelica*). The reasons for this choice were twofold. Firstly, much of the literature on xylem embolism seems to focus on the large vessel cells of angiosperms, which are thought to be mainly responsible for water transport instead of the smaller wood fibers, which are much smaller and more numerous (cf. figure 3). The two most common Finnish conifers (Norway spruce and Scots pine), on the other hand, have no vessels, but the xylem consists of only one axial cell type, tracheids. Secondly, the thick bark and branch structure of conifers would have been problematic in mounting the samples and choosing the proper imaging geometry.

The key result of paper **V** was to resolve three issues related to imaging live saplings with XMT:

1. Although the imaged stem section is only a few mm thick, a live sapling as a whole is fairly massive compared to the resolution of the imaging. This requires care in the sample mounting, as the imaged section has to remain fixed during the scan with micrometer precision, while at the same time avoiding the use of force in the mounting. In the paper, this issue was resolved by constructing a specific imaging pot, which had a metallic 'collar' around the bottom part of the stem to support the imaged section. The sample itself was attached to the holder at the top of the collar with beeswax.

2. With non-living samples, XMT is considered a non-destructive method, but in the case of live organisms, the ionizing radiation dose associated with the scan

might influence the behavior of the sample. Unfortunately, there is practically no literature on what the effects of such a localized dose would be on a tree, and even exact evaluation of the dose is difficult due to the point-like source and short source-to-sample distance. With careful optimization of the scan parameters, cross-sectional images with sufficient resolution were obtained in approximately 30 min, minimizing the radiation dose to the sample.

3. In order to use XMT to measure the degree of embolism in the stem, it is necessary to establish a quantitative data analysis method that yields a single number for comparison with PLC measurements. XMT does not differentiate between mobile and fixed water in the stem, so an exact match is impossible to achieve, but a similar measure for the amount of cavitation was used in paper **V**: PCS, or percentage of cavitated stem is simply the smallest singly connected cross sectional area where most xylem conduits are embolized divided by the total cross-sectional area. This was calculated instead by means of a volume propagation tool and morphological closing to reduce the sensitivity of the result to the chosen binarization threshold. Another important parameter would be the number of embolized vessel cells, which can simply be counted from a selected cross-sectional image. The quantification of xylem embolism in live tree saplings is illustrated figure 10.

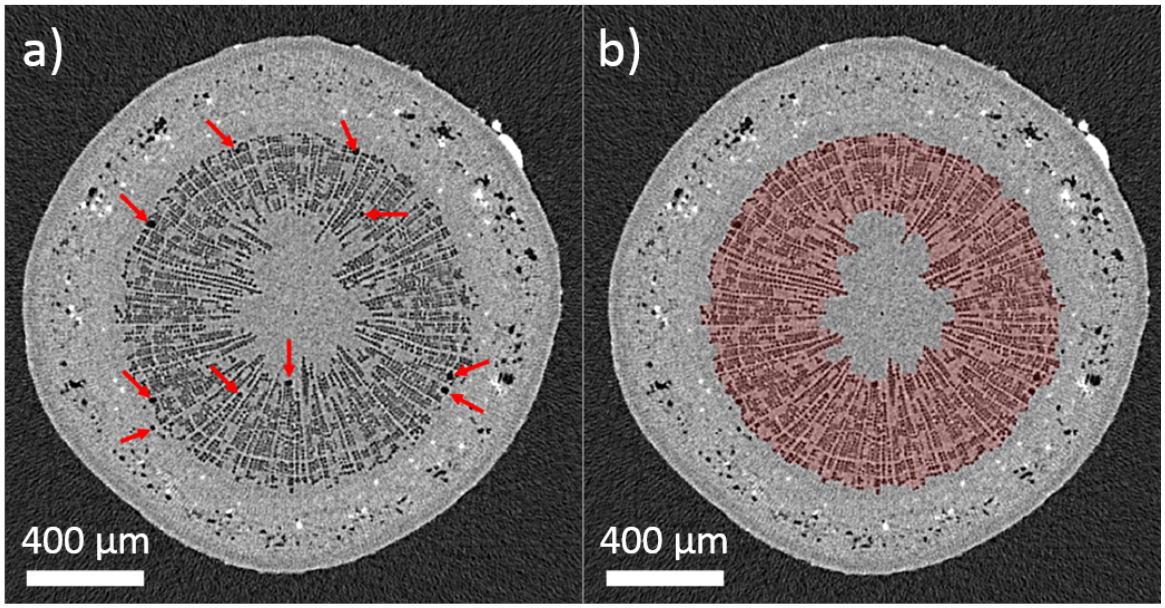


**Figure 10.** Quantification of xylem embolism in Silver and Curly birch saplings, as used in paper **V**. The number of embolized xylem vessels can be directly counted (red arrows in image **a)**), while the cross sectional area of primarily embolized tissue (red overlay in **b)**) was used as a measure of embolization in the wood fibers.

While the experiment successfully demonstrated the use of x-ray tube based XMT for visualizing the functional status of xylem conduits, the cross-sectional images obtained in the experiment seem puzzling in light of the established view of xylem embolism, where embolisms originate in the conducting vessels. Producing significant amounts of embolized vessels required a drought period of several days, while many wood fibers, especially near the middle of the stem, were cavitated already in well-watered plants. Drought conditions then resulted in loss of water from the fibers and the phloem before vessels were embolized. This could be due to a hydraulic capacitive effect (Scholz et al., 2011), where the xylem fibers and phloem act as an internal water source to the vessels during drought. However, further experiments would be necessary to validate this view of the drought response of *B. pendula*.

## 4.6 Steel fiber reinforced concrete

### 4.6.1 Background

The traditional way of reinforcing concrete structures in the construction industry is the use of steel reinforcement bars ('rebars'), which are positioned within the formwork prior to casting the concrete structural element. Installing the rebar cages, however, constitutes an additional step in the construction process, and rebars can be impractical in situations where the concrete layer is thin and/or irregularly shaped, such as using shotcrete for stabilizing tunnel walls or similar structures. An alternative method for increasing the strength and ductility of concrete is fiber reinforcement, in which the load-bearing elements are smaller and introduced to the concrete mass already at the mixing stage (Brandt, 2008). Steel, glass, or polymer fibers, among others, can be used for this purpose. Fiber composite materials besides concrete, such as carbon, glass or natural fiber polymers (Saheb and Jog, 1999; Williams et al., 2007) can also be used in many areas of engineering.

A downside of using fiber reinforced concrete is that the orientation of the fibers critically affects the properties of the composite (Barnett et al., 2010; Kang et al., 2011), and is more difficult to control than the orientation of rebars. Developing reliable methods for measuring the orientation distribution of the fibers is then crucial for designing and manufacturing load-bearing fiber reinforced concrete elements. In the case of steel fiber reinforced concrete (SFRC), average orientation can be measured through indirect methods (e.g. Faifer et al., 2011; Lataste et al., 2011), but x-ray CT is the only practical way to directly visualize the 3D fiber distribution in a representative sample of the finalized element. It is then a 3D image processing problem to quantify the fiber orientation distribution based on the reconstruction. How exactly to perform this quantification is an open problem common to all analyses of fibrous materials, and several approaches have been reported in the literature: Tan et al. (2006) used skeletonization of binarized XMT images to analyze bonded fiber networks, while Krause

et al. (2010) resort to determining a distribution of local orientation tensors, calculated at each fiber point without separation of individual fibers or fiber segments. A simple two-dimensional method analyzing only the elliptic cross-sections of fibers in a single slice was used by Barnett et al. (2010), similar to photometric analysis of cut drill core surfaces (Eik et al., 2013).

### 4.6.2 Aim and key results of the experiment

In paper **VI**, low-resolution XMT images (voxel size $\sim 130$ µm) were acquired of 10 cm drill cores taken from full-sized SFRC floor slabs, and analyzed with a custom designed image processing routine depicted in figure 11. The aim of the experiment was to explore the inhomogeneity of the fiber orientation within the floor slabs by analyzing samples taken from near the edge of the slabs as well as centrally located cores, and to evaluate the feasibility of the XMT analysis approach for wider implementation in e.g. quality control at element factories.

The data analysis proved to be challenging due to the low power of the XMT scanner, which is primarily designed for higher resolution scans of much less attenuating samples. In the case of SFRC, the poor x-ray penetration through the sample and beam hardening effects resulted in an array of artefacts (part 1. of figure 11) in the reconstruction, which were worked around by employing a 'highEdge' filter in the reconstruction software, replacing the $|w|$ in equation 7 by a function that overemphasizes high spatial frequencies. With the fiber diameter being relatively small, only a few times the voxel size, this resulted in images highlighting only the fibers and eliminated any radial intensity variation. The downside of the highEdge filtering was increased noise (also at high spatial frequency) in the reconstruction, which was in turn reduced by digital filtering of the reconstruction prior to the binarization step. After binarization, the morphological skeleton (Fouard et al., 2006) of the binary dataset was calculated, and processed with a custom MATLAB program in order to separate and label the fibers.

The results of the experiment demonstrate well the edge effect, or the tendency of fibers to align themselves with the formwork in samples drilled from near the edge of the slab. The difficulty of controlling fiber orientation is also evident from the results, as in most of the samples the fibers were neither randomly oriented, nor were they aligned in the direction of optimal reinforcement, which would have been the long axis of the floor slab. In conclusion, the spatial resolution of the used XMT setup was unnecessarily high, with a subsequent reduction of intensity, but the results give important guidelines for future work. Of particular interest is the presented fiber orientation analysis algorithm, which was found to give exceptionally accurate results when compared with a manual segmentation of one measured dataset. Moreover, much of the process could easily be automated if using an industrial CT scanner with lower maximum resolution but higher power.

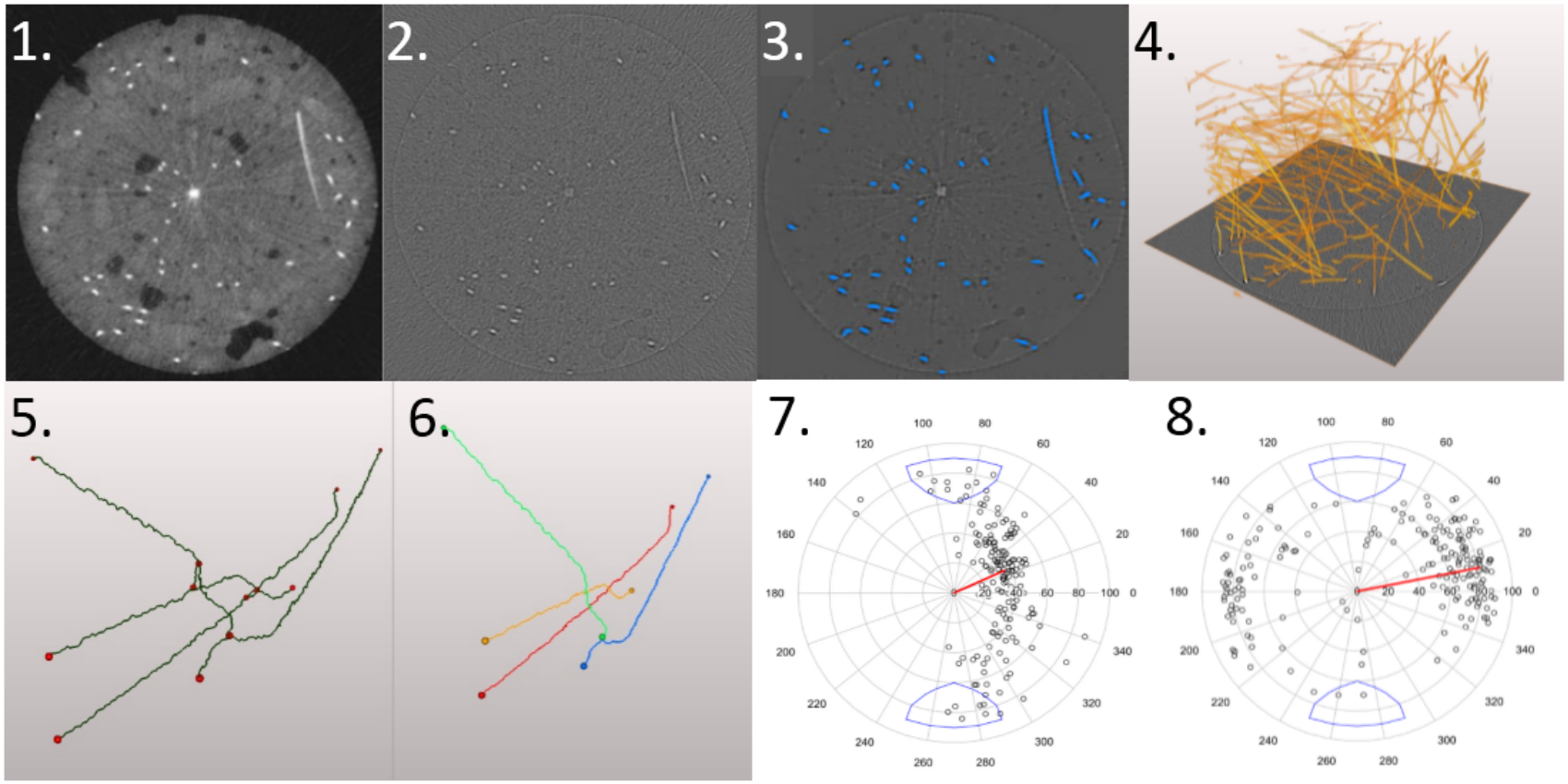


**Figure 11.** The algorithm used for quantification of fiber orientation from XMT data of steel fiber reinforced concrete in paper **VI**. **1.** and **2.**: An edge-enhancing filter (2.) was used instead of the standard (1.) filter at the reconstruction stage to yield images highlighting areas of high intensity variation (i.e. fibers). **3.** and **4.**: The edge enhanced reconstructions were further filtered digitally and binarized with a dual threshold algorithm to yield binary 3D images of only the fibers. **5.**: The binary images were skeletonized, or reduced to only the medial axes of the fibers. At this point groups of touching fibers like that shown in the image were still classified as a single object. **6.**: The medial axis data were processed with a self-written fiber separation algorithm that separates connected fibers based on the angles between connections and connection length. **7.** and **8.**: orientations of each individual fiber were determined and scatter plotted with distance from center corresponding to the deviation from vertical, and the azimuthal angle corresponding to the direction of the fiber in the plane of the slab. Blue markings correspond to the direction of optimal reinforcement. Image 7 shows results from a sample taken from near the edge of a floor slab, showing alignment of the fibers with the formwork surface. Image 8 represents a sample from the center of the slab.

# 5 Discussion and concluding remarks

In materials science and many other fields (excluding medicine), the introduction of microtomography equipment based on micro- and nanofocus x-ray tubes has taken three dimensional x-ray imaging from being a marginal technique only available at synchrotron facilities into a maturing technology that is accessible and in routine use at numerous research institutes and universities. The improving resolution of XMT equipment has opened up a wide array of problems into which three-dimensional images of the internal microstructure of the sample can shed new light. However, every application field poses its own unique set of questions to be addressed before a new method can be adopted as a standard practice. In the case of XMT, these issues may be technical in nature, relating to proper sample handling and selection of scan parameters, but usually accompanied by a data analysis problem: how to best extract relevant scientific information from the 3D image. It is also very often the case, that 3D imaging provides fundamentally different information from the traditional experimental methods in the field, and part of the challenge is establishing a link between the two.

In this thesis, papers **V** and **VI** represent tackling these challenges in two very different fields. In the issue of xylem embolism (paper **V**), the essential aspect that makes XMT highly useful is the non-destructivity. All of the established methods used to quantify the phenomenon involve cutting the plant, which makes them vulnerable to artifical cavitation produced in the sampling. Recent research in the field has questioned the existing views of high vulnerability to cavitation and diurnal cavitation and refilling cycles in some species (Rockwell et al., 2014), and advocated using XMT as a reference method for detecting cavitation *in vivo* (Brodersen, 2013; Cochard et al., 2014). While using XMT for imaging live plants is necessarily limited to young trees, and even then some practical challenges undoubtedly will arise when more species need to be studied, the major issue in this field will be finding out how the observed cavitation patterns are related to the hydraulic conductivity of the stem.

Imaging the fibers inside SFRC samples is technically straightforward; the difficulty lies in the data analysis part of the experiment. Paper **VI** is largely devoted to developing the necessary data analysis workflow for analyzing the fiber orientation distribution in SFRC, but the presented algorithm could, at least in part, be easily applied to other fiber composite materials as well. While the procedure is fairly complex, up to the fiber separation algorithm it mainly consists of standard image processing tools available on many different software platforms. Using data from a more powerful, lower resolution XMT scanner, readily available on the market, would also facilitate automation of the process, which is an important consideration if such an analysis is to be utilized in an industrial setting. The fiber separation algorithm in itself is also somewhat parallelizable, as each cluster of fibers is processed separately. Also in this field, the ultimate questions nevertheless concern the link between the structural data gained with XMT

and the properties of the final macroscopic system: a constitutive relationship between fiber orientation and the mechanical properties of the floor slab (Herrmann et al., 2014), and developing a manufacturing method that enables controlling the fiber orientation.

The success, and especially the limitations, of conventional x-ray attenuation microtomography in various fields have also been driving the development of the methodology itself. The poor contrast of conventional XMT with low-density materials composed of light elements can be remedied by using phase contrast imaging. At present, phase contrast microtomography is a routine experiment at most synchrotron facilities, and starting from lower resolution equipment, phase contrast is finding its way into x-ray tube based scanners as well (Bech et al., 2009; Pfeiffer et al., 2006). Another avenue of improvement for the methodology has been in developing sample stages to allow monitoring the sample in changing, or extreme, environmental conditions. An XMT scanner is quite challenging in this respect, since the sample holder should preferably be x-ray transparent on all sides. A simple example of such development is the holder used for humidity control in paper **IV**.

A third important methodological example is incorporating other x-ray methods into the analysis, either as an alternative contrast mechanism, or as complementary information to an attenuation or phase contrast XMT image. In this endeavor, the greater brilliance and monochromaticity of synchrotron sources provides unmatched possibilities in terms of resolution (both spatial and temporal), but adopting similar methods for use with x-ray tube instruments will make them available in a much wider range of topics, not all of which require extremely high resolution. This is exemplified in papers **I** – **IV** of the thesis, utilizing both x-ray scattering and XMT as complementary structural probes. The non-destructive nature of x-rays are a distinctive advantage also in the scattering experiments: in the micrometeorite experiment (paper **III**), the rare samples were preserved for further experiments, and in the clay experiment of paper **IV**, the non-destructivity allowed making measurements on exactly the same pieces at varying humidity levels, eliminating any effects of possible heterogeneity in the samples. The novel feature of the present work is the combination of XMT and x-ray diffraction in a single bench-top instrument. A region of interest within the sample can be selected based on the XMT scan, and transferred to coincide with the x-ray beam of the scattering experiment. This enables correlating the micrometer-level morphology of the sample with nanoscale structural properties, providing unique information across length scales.

# References

Allen, C. D. et al. (2010). A global overview of drought and heat-induced tree mortality reveals emerging climate change risks for forests. *Forest Ecology and Management*, 259(4):660 – 684. Adaptation of Forests and Forest Management to Changing Climate - Selected papers from the conference on "Adaptation of Forests and Forest Management to Changing Climate with Emphasis on Forest Health: A Review of Science, Policies and Practices", Umeå, Sweden, August 25-28, 2008.

Álvarez-Murga, M., Bleuet, P., and Hodeau, J.-L. (2012). Diffraction/scattering computed tomography for three-dimensional characterization of multi-phase crystalline and amorphous materials. *Journal of Applied Crystallography*, 45:1109–1124.

Andra (2013). The Cigeo project: Meuse/Haute-Marne reversible geological disposal facility for radioactive waste. Technical Report 504VA DCOM/13-0271, Andra — French National Agency for Radioactive Waste Management, Châtenau-Malabry, France.

Auclair, A. N. D. (1993). Extreme climatic fluctuations as a cause of forest diebacks in the pacific rim. *Water, Air, and Soil Pollution*, 66:207–229.

Banhart, J., editor (2008). *Advanced Tomographic Methods in Materials Research and Engineering*. Oxford University Press, New York.

Bare, S. R., Charochak, M. E., Kelly, S. D., Lai, B., Wang, J., and Chen-Wiegart, Y.-c. K. (2014). Characterization of a Fluidized Catalytic Cracking Catalyst on Ensemble and Individual Particle Level by X-ray Micro- and Nanotomography, Micro-X-ray Fluorescence, and Micro-X-ray Diffraction. *ChemCatChem*, 6(5):1427–1437.

Barnett, S. J., Lataste, J.-F., Parry, T., Millard, S. G., and Soutsos, M. N. (2010). Assessment of fibre orientation in ultra high performance fibre reinforced concrete and its effect on flexural strength. *Materials and Structures*, 43(7):1009–1023.

Barrett, J. F. and Keat, N. (2004). Artifacts in CT: Recognition and Avoidance. *Radiographics*, 24:1679–1691.

Bech, M., Jensen, T. H., Feidenhans'l, R., Bunk, O., David, C., and Pfeiffer, F. (2009). Soft-tissue phase-contrast tomography with an x-ray tube source. *Physics in Medicine and Biology*, 54(9):2747.

Bergaya, F. and Lagaly, G. (2013). Chapter 1 - general introduction: Clays, clay minerals, and clay science. In Bergaya, F. and Lagaly, G., editors, *Handbook of Clay Science*, volume 5 of *Developments in Clay Science*, pages 1 – 19. Elsevier.

Bleuet, P., Welcomme, E., Dooryhée, E., Susini, J., Hodeau, J.-L., and Walter, P. (2008). Probing the structure of heterogeneous diluted materials by diffraction tomography. *Nature Materials*, 7:468–472.

Brandt, A. M. (2008). Fibre reinforced cement-based (FRC) composites after over 40 years of development in building and civil engineering. *Composite Structures*, 86(13):3 – 9. Fourteenth International Conference on Composite Structures ICCS/14.

Brigatti, M., Galán, E., and Theng, B. (2013). Chapter 2 - Structure and Mineralogy of Clay Minerals. In Bergaya, F. and Lagaly, G., editors, *Handbook of Clay Science*, volume 5 of *Developments in Clay Science*, pages 21 – 81. Elsevier.

Brodersen, C. (2013). Visualizing wood anatomy in three dimensions with high-resolution X-ray micro-tomography (µCT) — A review. In *Wood Structure in Plant Biology and Ecology*, pages 80–96.

Brodersen, C. R., McElrone, A. J., Choat, B., Lee, E. F., Shackel, K. A., and Matthews, M. A. (2013). In vivo visualizations of drought-induced embolism spread in *Vitis vinifera*. *Plant Physiology*, 161:1820–1829.

Brodersen, C. R., McElrone, A. J., Choat, B., Matthews, M. A., and Shackel, K. A. (2010). The dynamics of embolism repair in xylem: In vivo visualizations using high-resolution computed tomography. *Plant Physiology*, 154:1088–1095.

Buffiere, J.-Y., Maire, E., Adrien, J., Masse, J.-P., and Boller, E. (2010). *In situ* experiments with x ray tomography: An attractive tool for experimental mechanics. *Experimental Mechanics*, 50:289–305.

Bushberg, J. T., Seibert, J. A., Leidholt, Jr., E. M., and Boone, J. M. (2002). *The Essential Physics of Medical Imaging*. Lippincott Williams & Wilkins, Philadelphia, 2. edition. s. 327-329.

Buzug, T. M. (2008). *Computed Tomography, From Photon Statistics to Modern Cone-Beam CT*. Springer-Verlag.

Canny, M. J. and Huang, C. X. (2001). The cohesion theory debate continues. *Trends in Plant Science*, 6(10):454–455.

Choat, B., Drayton, W. M., Brodersen, C., Matthews, M. A., Shackel, K. A., Wada, H., and McElrone, A. J. (2010). Measurement of vulnerability to water stress-induced cavitation in grapevine: a comparison of four techniques applied to a long-vesseled species. *Plant, Cell & Environment*, 33(9):1502–1512.

Cloetens, P., Ludwig, W., Baruchel, J., Van Dyck, D., Van Landuyt, J., Guigay, J. P., and Schlenker, M. (1999). Holotomography: Quantitative phase tomography with micrometer resolution using hard synchrotron radiation x rays. *Applied Physics Letters*, 75(19):2912–2914.

Cnudde, V., Masschaele, B., Dierick, M., Vlassenbroeck, J., Van Hoorebecke, L., and Jacobs, P. (2006). Recent progress in X-ray CT as a geosciences tool. *Applied Geochemistry*, 21:826–832.

Cochard, H., Améglio, T., and Cruiziat, P. (2001). The cohesion theory debate continues. *Trends in Plant Science*, 6(10):456.

Cochard, H., Delzon, S., and Badel, E. (2014). X-ray microtomography (micro-CT): a reference technology for high-resolution quantification of xylem embolism in trees. *Plant, Cell & Environment*. DOI: 10.1111/pce.12391.

Consolmagno, G., Britt, D., and Macke, R. (2008). The significance of meteorite density and porosity. *Chemie der Erde - Geochemistry*, 68(1):1 – 29.

Cruiziat, P. and Richter, H. (2006). Essay 4.2, the cohesion-tension theory at work. Online appendix to Taiz and Zeiger (2010). `http://5e.plantphys.net/categories.php?t=e` Accessed 06.08.2014.

Cullity, B. and Stock, S. (2001). *Elements of x-ray diffraction*. Prentice Hall, Upper Saddle River, New Jersey, 3rd edition.

de Paiva, L. B., Morales, A. R., and Daz, F. R. V. (2008). Organoclays: Properties, preparation and applications. *Applied Clay Science*, 42(12):8 – 24.

Derome, D., Griffa, M., Koebel, M., and Carmeliet, J. (2011). Hysteretic swelling of wood at cellular scale probed by phase-contrast x-ray tomography. *Journal of Structural Biology*, 173:180–190.

Devineau, K., Bihannic, I., Michot, L., Villerás, F., Masrouri, F., Cuisinier, O., Fragneto, G., and Michau, N. (2006). In situ neutron diffraction analysis of the influence of geometric confinement on crystalline swelling of montmorillonite. *Applied Clay Science*, 31:76–84.

DeVore, M. L., Kenrick, P., Pigg, K. B., and Ketcham, R. A. (2006). Utility of high resolution x-ray computed tomography (HRXCT) for paleobotanical studies: an example using London Clay fruits and seeds. *American Journal of Botany*, 93(12):1848–1851.

Dohrmann, R., Kaufhold, S., and Lundqvist, B. (2013). Chapter 5.4 - the role of clays for safe storage of nuclear waste. In Bergaya, F. and Lagaly, G., editors, *Handbook of Clay Science*, volume 5 of *Developments in Clay Science*, pages 677 – 710. Elsevier.

Eik, M., Lõhmus, K., Tigasson, M., Listak, M., Puttonen, J., and Herrmann, H. (2013). DC-conductivity testing combined with photometry for measuring fibre orientations in SFRC. *Journal of Materials Science*, 48(10):3745–3759.

Faifer, M., Ottoboni, R., Toscani, S., and Ferrara, L. (2011). Nondestructive testing of steel-fiber-reinforced concrete using a magnetic approach. *Instrumentation and Measurement, IEEE Transactions on*, 60(5):1709–1717.

Feldkamp, L., Davis, L., and Kress, J. (1984). Practical cone-beam algorithm. *Journal of the Optical Society of America*, 1(6):612–619.

Ferrage, E., Lanson, B., Sakharov, B., and Drits, V. (2005). Investigation of smectite hydration properties by modling experimental X-ray diffraction patterns. Part I. Montmorillonite hydration properties. *American Mineralogist*, 90(8-9):1358–1374.

Flannery, B. P., Deckman, H. W., Roberge, W. G., and D'Amico, K. L. (1987). Three-dimensional x-ray microtomography. *Science*, 237:1439–1444.

Fouard, C., Malandain, G., Prohaska, S., and Westerhoff, M. (2006). Blockwise processing applied to brain microvascular network study. *Medical Imaging, IEEE Transactions on*, 25(10):1319–1328.

Friedrich, J. M., Wignarajah, D. P., Chaudhary, S., Rivers, M. L., Nehru, C., and Ebel, D. S. (2008). Three-dimensional petrography of metal phases in equilibrated L. chondrites — Effects of shock loading and dynamic compaction. *Earth and Planetary Science Letters*, 275:172–180.

Fuloria, D. and Lee, P. (2009). An X-ray microtomographic and finite element modeling approach for the prediction of semi-solid deformation behaviour in AlCu alloys. *Acta Materialia*, 57(18):5554 – 5562.

Gardelle, B., Duquesne, S., Vandereecken, P., Bellayer, S., and Bourbigot, S. (2013). Resistance to fire of intumescent silicone based coating: The role of organoclay. *Progress in Organic Coatings*, 76(11):1633 – 1641.

Genge, M. J., Engrand, C., Gounelle, M., and Taylor, S. (2008). The classification of micrometeorites. *Meteoritics & Planetary Science*, 43(3):497–515.

Ghiaci, M., Aghabarari, B., and Gil, A. (2011). Production of biodiesel by esterification of natural fatty acids over modified organoclay catalysts. *Fuel*, 90(11):3382 – 3389.

Gonzalez, R. C. and Woods, R. E. (2002). *Digital Image Processing*. Prentice Hall, 2. edition.

Gopakumar, T., Lee, J., Kontopoulou, M., and Parent, J. (2002). Influence of clay exfoliation on the physical properties of montmorillonite/polyethylene composites. *Polymer*, 43(20):5483 – 5491.

Herrmann, H., Eik, M., Berg, V., and Puttonen, J. (2014). Phenomenological and numerical modelling of short fibre reinforced cementitious composites. *Meccanica*, 49(8):1985–2000.

Hezel, D. C., Elangovan, P., Viehmann, S., Howard, L., Abel, R. L., and Armstrong, R. (2013). Visualisation and quantification of CV chondrite petrography using microtomography. *Geochimica et Cosmochimica Acta*, 116(0):33 – 40. Looking Inside: 3D Structures of Meteorites.

Holbrook, N. M., Ahrens, E. T., Burns, M. J., and Zwieniecki, M. A. (2001). In vivo observation of cavitation and embolism repair using magnetic resonance imaging. *Plant Physiology*, 126:27–31.

Holbrook, N. M. and Zwieniecki, M. A. (1999). Embolism repair and xylem tension: Do we need a miracle? *Plant Physiology*, 120:7–10.

Hounsfield, G. N. (1973). Computerized transverse axial scanning (tomography): Part 1. Description of system. *The British Journal of Radiology*, 46(552):1016–1022.

Huang, T. C., Toraya, H., Blanton, T. N., and Wu, Y. (1993). X-ray powder diffraction analysis of silver behenate, a possible low-angle diffraction standard. *Journal of Applied Crystallography*, 26(2):180–184.

Huotari, S., Pylkkänen, T., Verbeni, R., Monaco, G., and Hämäläinen, K. (2011). Direct tomography with chemical-bond contrast. *Nature Materials*, 10:489–493.

Jang, B., Kaeli, D., Do, S., and Pien, H. (2009). Multi GPU implementation of iterative tomographic reconstruction algorithms. In *Biomedical Imaging: From Nano to Macro, 2009. ISBI '09. IEEE International Symposium on*, pages 185–188.

Johnson, G., King, A., Honnicke, M. G., Marrow, J., and Ludwig, W. (2008). X-ray diffraction contrast tomography: a novel technique for three-dimensional grain mapping of polycrystals. II. The combined case. *Journal of Applied Crystallography*, 41(2):310–318.

Jones, T. (1983). The properties and uses of clays which swell in organic solvents. *Clay Minerals*, 18:399–410.

Juvankoski, M. (2013). Buffer design 2012. Technical Report Posiva 2012-14, Posiva Oy, Eurajoki, Finland.

Kak, A. C. and Slaney, M. (2001). *Principles of Computerized Tomographic Imaging*. SIAM Society for Industrial and Applied Mathematics. Re-publication of original work in 1988 (IEEE Press, New York).

Kang, S. T., Lee, B. Y., Kim, J.-K., and Kim, Y. Y. (2011). The effect of fibre distribution characteristics on the flexural strength of steel fibre-reinforced ultra high strength concrete. *Construction and Building Materials*, 25(5):2450 – 2457.

Keller, L. M., Holzer, L., Wepf, R., and Gasser, P. (2011). 3D geometry and topology of pore pathways in Opalinus Clay: Implications for mass transport. *Applied Clay Science*, 52:85–95.

King, A., Reischig, P., Adrien, J., and Ludwig, W. (2013). First laboratory x-ray diffraction contrast tomography for grain mapping of polycrystals. *Journal of Applied Crystallography*, 46(6):1734–1740.

Kondo, M., Tsuchiyama, A., Hirai, H., and Koishikawa, A. (1997). High resolution X-ray computed tomographic (CT) images of chondrites and a chondrule. *Antarctic Meteorite Research*, 10:437–447.

Krause, M., Hausherr, J., Burgeth, B., Herrmann, C., and Krenkel, W. (2010). Determination of the fibre orientation in composites using the structure tensor and local x-ray transform. *Journal of Materials Science*, 45(4):888–896.

Lagaly, G., Ogawa, M., and Dkny, I. (2013). Chapter 10.3 - Clay Mineral-Organic Interactions. In Bergaya, F. and Lagaly, G., editors, *Handbook of Clay Science*, volume 5 of *Developments in Clay Science*, pages 435 – 505. Elsevier.

Lambert, J.-F. and Bergaya, F. (2013). Chapter 13.1 - Smectite-Polymer Nanocomposites. In Bergaya, F. and Lagaly, G., editors, *Handbook of Clay Science*, volume 5 of *Developments in Clay Science*, pages 679 – 706. Elsevier.

Lataste, J., Barnett, S. J., Parry, T., and Soutsos, M. N. (2011). Study of fibre distribution and orientations in UHPFRC by electrical resistivity and mechanical tests. *European Journal of Environmental and Civil Engineering*, 15(4):533–544.

Leppänen, K., Bjurhager, I., Peura, M., Kallonen, A., Suuronen, J.-P., Penttilä, P., Love, J., Fagerstedt, K., and Serimaa, R. (2011). X-ray scattering and microtomography study on the structural changes of never-dried silver birch, european and hybrid aspen during drying. *Holzforschung*, 65:865–873.

Ludwig, W., King, A., Herbig, M., Reischig, P., Marrow, J., Babout, L., Lauridsen, E., Proudhon, H., and Buffière, J. (2012). Characterization of polycrystalline materials using synchrotron x-ray imaging and diffraction techniques. *JOM*, 62(12):22–28.

Ludwig, W., Schmidt, S., Lauridsen, E. M., and Poulsen, H. F. (2008). X-ray diffraction contrast tomography: a novel technique for three-dimensional grain mapping of polycrystals. I. Direct beam case. *Journal of Applied Crystallography*, 41(2):302–309.

Macke, R. J., Britt, D. T., and Consolmagno, G. J. (2010). Analysis of systematic error in bead method measurements of meteorite bulk volume and density. *Planetary and Space Science*, 58(3):421 – 426.

Maire, E. (2012). X-ray tomography applied to the characterization of highly porous materials. *Annual Review of Materials Research*, 42:163–78.

Martin, T. and Koch, A. (2006). Recent developments in x-ray imaging with micrometer spatial resolution. *Journal of Synchrotron Radiation*, 13:180–194.

Martínez-Criado, G., Tucoulou, R., Cloetens, P., Bleuet, P., Bohic, S., Cauzid, J., Kieffer, I., Kosior, E., Labouré, S., Petitgirard, S., Rack, A., Sans, J., Segura-Ruiz, J., Suhonen, H., Susini, J., and Villanova, J. (2012). Status of the hard X-ray microprobe beamline ID22 of the European Synchrotron Radiation Facility. *Journal of Synchrotron Radiation*, 19:10–18.

Mayo, S., Davis, T., Gureyev, T., Miller, P., Paganin, D., Pogany, A., Stevenson, A., and Wilkins, S. (2003). X-ray phase-contrast microscopy and microtomography. *Optics Express*, 11(19):2289–2302.

McCausland, P. J. A., Samson, C., and McLeod, T. (2011). Determination of bulk density for small meteorite fragments via visible light 3-D laser imaging. *Meteoritics & Planetary Science*, 46(8):1097–1109.

Menon, M., Yuan, Q., Jia, X., Dougill, A., Hoon, S., Thomas, A., and Williams, R. (2011). Assessment of physical and hydrological properties of biological soil crusts using x-ray microtomography and modeling. *Journal of Hydrology*, 397(12):47 – 54.

Mikkonen, K., Parikka, K., Suuronen, J.-P., Ghafar, A., Serimaa, R., and Tenkanen, M. (2014). Enzymatic oxidation as a potential new route to produce polysaccharide aerogels. *RSC Advances*, 4:11884.

Mote, A. S., Ketcham, R. A., and Watson, W. P. (2010). Extracting Particle Orientations from Three-dimensional Datasets using BLOB3D. In *Advances in X-ray Tomography for Geomaterials*, pages 407–413. ISTE.

Myers, G., Mayo, S., Gureyev, T., Paganin, D., and Wilkins, S. (2007). Polychromatic cone-beam phase-contrast tomography. *Physical Review A*, 76:045804.

Nagra (2002). Opalinus Clay Project, Demonstration of feasibility of disposal (Entsorgungsnachweis) for spent fuel, vitrified high-level waste and long-lived intermediate-level waste, Summary Overview. Technical report, Nagra Swiss National Cooperative for the Disposal of Radioactive Waste, Wettingen, Switzerland.

Naik, N., Jupe, A., Stock, S., Wilkinson, A., Lee, P., and Kurtis, K. (2006). Sulfate attack monitored by microCT and EDXRD: Influence of cement type, water-to-cement ratio, and aggregate. *Cement and Concrete Research*, 36:144–159.

Nakamura, T., Tsuchiyama, A., Akaki, T., Uesugi, K., Nakano, T., Takeuchi, A., Suzuki, Y., and Noguchi, T. (2008). Bulk mineralogy and three-dimensional structures of individual Stardust particles deduced from synchrotron X-ray diffraction and microtomography analysis. *Meteoritics & Planetary Science*, 43(1-2):247–259.

Nesvorný, D., Jenniskens, P., Levison, H. F., Bottke, W. F., Vokrouhlický, D., and Gounelle, M. (2010). Cometary origin of the zodiacal cloud and carbonaceous micrometeorites. Implications for hot debris disks. *The Astrophysical Journal*, 713(2):816.

Nesvorný, D., Vokrouhlický, D., Bottke, W. F., and Sykes, M. (2006). Physical properties of asteroid dust bands and their sources. *Icarus*, 181(1):107 – 144.

Ogasa, M., Miki, N., Okamoto, M., Yamanaka, N., and Yoshikawa, K. (2014). Water loss regulation to soil drought associated with xylem vulnerability to cavitation in temperate ring-porous and diffuse-porous tree seedlings. *Trees*, 28(2):461–469.

Ogasa, M., Miki, N., and Yoshikawa, K. (2010). Changes of hydraulic conductivity during dehydration and rehydration in *Quercus serrata* Thunb. and *Betula platyphylla* var. *japonica* Hara: the effect of xylem structures. *Tree Physiology*, 30:608–617.

Ohser, J. and Schladitz, K. (2009). *3D Images of Material Structures*. Wiley-VCH, Weinheim, Germany.

Otsu, N. (1979). A threshold selection method from gray-level histograms. *Systems, Man and Cybernetics, IEEE Transactions on*, 9(1):62–66.

Paul, D. and Robeson, L. (2008). Polymer nanotechnology: Nanocomposites. *Polymer*, 49(15):3187 – 3204.

Penttilä, P., Kilpeläinen, P., Tolonen, L., Suuronen, J.-P., Sixta, H., Willför, S., and Serimaa, R. (2013). Effects of pressurized hot water extraction on the nanoscale structure of birch sawdust. *Cellulose*, 20(5):2335–2347.

Pfeiffer, F., Weitkamp, T., Bunk, O., and David, C. (2006). Phase retrieval and differential phase-contrast imaging with low-brilliance x-ray sources. *Nature Physics*, 2:258–261.

Pinto, C. A., David, J. S., Cochard, H., Caldeira, M. C., Henriques, M. O., Quilhó, T., Paço, T. A., Pereira, J. S., and David, T. S. (2012). Drought-induced embolism in current-year shoots of two mediterranean evergreen oaks. *Forest Ecology and Management*, 285(0):1 – 10.

Posiva (2012). Safety case for the disposal of spent nuclear fuel at Olkiluoto — Synthesis 2012. Technical Report Posiva 2012-12, Posiva Oy, Eurajoki, Finland.

Rack, A., Garcia-Moreno, F., Schmitt, C., Betz, O., Cecilia, A., Ershov, A., Rack, T., Banhart, J., and Zabler, S. (2010). On the possibilities of hard x-ray imaging with high spatio-temporal resolution using polychromatic synchrotron radiation. *Journal of X-ray Science and Technology*, 18:429–441.

Radon, J. (1986). On the determination of functions from their integral values along certain manifolds. *Medical Imaging, IEEE Transactions on*, 5(4):170–176.

Ramachandran, G. N. and Lakshminarayanan, A. V. (1971). Three-dimensional reconstruction from radiographs and electron micrographs: Application of convolutions instead of Fourier transforms. *Proceedings of the National Academy of Sciences*, 68(9):2236–2240.

Rockwell, F. E., Wheeler, J. K., and Holbrook, N. M. (2014). Cavitation and its discontents: Opportunities for resolving current controversies. *Plant Physiology*, 164(4):1649–1660.

Röntgen, W. K. (1896). On a new kind of rays. *Nature*, 53(1369):274–276.

Saheb, D. and Jog, J. (1999). Natural fiber polymer composites: A review. *Advances in Polymer Technology*, 18(4):351–363.

Salleo, S., Lo Gullo, M., Trifilò, P., and Nardini, A. (2004). New evidence for a role of vessel-associated cells and phloem in the rapid xylem refilling of cavitated stems of *Laurus nobilis* L. *Plant, Cell and Environment*, 27:1065–1076.

Sano, Y., Okamura, Y., and Utsumi, Y. (2005). Visualizing water-conduction pathways of living trees: selection of dyes and tissue preparation methods. *Tree Physiology*, 25(3):269–275.

Sato, H. and Suzuki, S. (2003). Fundamental study on the effect of an orientation of clay particles on diffusion pathway in compacted bentonite. *Applied Clay Science*, 23:51–60.

Schindelin, J., Arganda-Carreras, I., Frise, E., Kaynig, V., Longair, M., Pietzsch, T., Preibisch, S., Rueden, C., Saalfeld, S., Schmid, B., et al. (2012). Fiji: an open-source platform for biological-image analysis. *Nature methods*, 9(7):676–682.

Scholz, F. G., Phillips, N. G., Bucci, S. J., Meinzer, F. C., and Goldstein, G. (2011). Hydraulic capacitance: Biophysics and functional significance of internal water sources in relation to tree size. In Meinzer, F. C., Lachenbruch, B., and Dawson, T. E., editors, *Size- and Age-Related Changes in Tree Structure and Function*, volume 4 of *Tree Physiology*, pages 341–361. Springer Netherlands.

Schroer, C. G., Kuhlmann, M., Roth, S. V., Gehrke, R., Stribeck, N., Almendarez-Camarillo, A., and Lengeler, B. (2006). Mapping the local nanostructure inside a specimen by tomographic small-angle x-ray scattering. *Applied Physics Letters*, 88(16):164102.

Siengchin, S., Karger-Kocsis, J., Apostolov, A., and Thomann, R. (2007). Polystyrene-fluorohectorite nanocomposites prepared by melt mixing with and without latex precompounding: Structure and mechanical properties. *Journal of Applied Polymer Science*, 106:248–254.

Siltanen, S. and Mueller, J. (2012). *Linear and Nonlinear Inverse Problems with Practical Applications*. SIAM.

SKB (2011). Long-term safety for the final repository for spent nuclear fuel at Forsmark. Main report of the SR-Site project. Technical Report SKB TR-11-01, Svensk Kärnbränslehantering Ab, Stockholm, Sweden.

Sperry, J. (2013). Cutting-edge research or cutting-edge artefact? An overdue control experiment complicates the xylem refilling story. *Plant, Cell & Environment*, 36(11):1916–1918.

Sperry, J. S., Nichols, K. L., Sullivan, J. E. M., and Eastlack, S. E. (1994). Xylem embolism in ring-porous, diffuse-porous, and coniferous trees of northern utah and interior alaska. *Ecology*, 75(6):1736–1752.

Stock, S., Barss, J., Dahl, T., Veis, A., and Almer, J. (2002). X-ray absorption microtomography (microCT) and small beam diffraction mapping of sea urchin teeth. *Journal of Structural Biology*, 139:1–12.

Stock, S. R. (2006). Combining absorption microCT and position-resolved x-ray scattering. In *Proc. SPIE*, volume 6318, pages 631816–631816–8.

Stock, S. R. (2009). *Microcomputed Tomography, Methodology and Applications*. CRC Press.

Suzuki, S., Sato, H., Ishidera, T., and Fujii, N. (2004). Study on anisotropy of effective diffusion coefficient and activation energy for deuterated water in compacted sodium bentonite. *Journal of Contaminant Hydrology*, 68:23–37.

Svedström, K., Bjurhager, I., Kallonen, A., Peura, M., and Serimaa, R. (2012). Structure of oak wood from the Swedish warship Vasa revealed by X-ray scattering and microtomography. *Holzforschung*, 66:355–363.

Taiz, L. and Zeiger, E. (2010). *Plant Physiology*. Sinauer Associates Inc., Sunderland, Massachusetts, 5. edition.

Tan, J., Elliott, J., and Clyne, T. (2006). Analysis of tomography images of bonded fibre networks to measure distributions of fibre segment length and fibre orientation. *Advanced Engineering Materials*, 8(6):495–500.

Taylor, S., Jones, K. W., Herzog, G. F., and Hornig, C. E. (2011). Tomography: A window on the role of sulfur in the structure of micrometeorites. *Meteoritics & Planetary Science*, 46(10):1498–1509.

Tomasi, C. and Manduchi, R. (1998). Bilateral filtering for gray and color images. In *Proceedings of the 1998 IEEE International Conference on Computer Vision*, pages 839–846.

Trtik, P., Dual, J., Keunecke, D., Mannes, D., Niemz, P., Stähli, P., Kaestner, A., Groco, A., and Stampanoni, M. (2007). 3D imaging of microstructure of spruce wood. *Journal of Structural Biology*, 159:46–55.

Turbell, H. (2001). *Cone-Beam Reconstruction Using Filtered Backprojection*. PhD thesis, Linköpings Universitet.

Utsumi, Y. and Sano, Y. (2007). Cryoplaning technique for visualizing the distribution of water in woody tissues by cryoscanning electron microscopy. In Kuo, J., editor, *Electron Microscopy*, volume 369 of *Methods in Molecular Biology*, pages 497–506. Humana Press.

Viani, A., Gualtieri, A. F., and Artioli, G. (2002). The nature of disorder in montmorillonite by simulation of x-ray powder patterns. *American Mineralogist*, 87(7):966–975.

Wagner, J.-F. (2013). Chapter 5.3 - clay liners and waste disposal. In Bergaya, F. and Lagaly, G., editors, *Handbook of Clay Science*, volume 5 of *Developments in Clay Science*, pages 663 – 676. Elsevier.

Wenk, H.-R., Voltolini, M., Mazurek, M., Van Loon, L., and Vinsot, A. (2008). Preferred orientations and anisotrpoy in shales: Callovo-Oxfordian shale (France) and Opalinus clay (Switzerland). *Clays and Clay Minerals*, 56(3):285–306.

Wheeler, J. K. and Holbrook, M. N. (2007). Essay 4.4, cavitation and refilling. Online appendix to Taiz and Zeiger (2010). `http://5e.plantphys.net/categories.php?t=e` Accessed 06.08.2014.

Williams, G., Trask, R., and Bond, I. (2007). A self-healing carbon fibre reinforced polymer for aerospace applications. *Composites Part A: Applied Science and Manufacturing*, 38(6):1525 – 1532.

Xu, F. and Mueller, K. (2005). Accelerating popular tomographic reconstruction algorithms on commodity PC graphics hardware. *Nuclear Science, IEEE Transactions on*, 52(3):654–663.